nature microbiology

Article

https://doi.org/10.1038/s41564-025-02030-7

Viral evolution prediction identifies broadly neutralizing antibodies to existing and prospective SARS-CoV-2 variants

Received: 29 September 2024

Accepted: 8 May 2025

Published online: 10 June 2025

Check for updates

Fanchong Jian[1,2,3,11], Anna Z. Wec[4,11], Leilei Feng[5,6,11], Yuanling Yu[2], Lei Wang[5,6], Peng Wang[2], Lingling Yu[2], Jing Wang[1,2,7], Jacob Hou[4], Daniela Montes Berrueta[4], Diana Lee[4], Tessa Speidel[4], LingZhi Ma[4], Thu Kim[4], Ayijiang Yisimayi[1,2,7], Weiliang Song[1,2,7], Jing Wang[2], Lu Liu[2], Sijie Yang[1,8], Xiao Niu[1,3], Tianhe Xiao[1,9], Ran An[2], Yao Wang[2], Fei Shao[2], Youchun Wang[2,10], Simone Pecetta[4], Xiangxi Wang[5,6] ✉, Laura M. Walker[4] ✉ & Yunlong Cao[1,2,8] ✉

Monoclonal antibodies (mAbs) targeting the SARS-CoV-2 receptor-binding domain are used to treat and prevent COVID-19. However, the rapid evolution of SARS-CoV-2 drives continuous escape from therapeutic mAbs. Therefore, the ability to identify broadly neutralizing antibodies (bnAbs) to future variants is needed. Here we use deep mutational scanning to predict viral receptor-binding domain evolution and to select for mAbs neutralizing both existing and prospective variants. A retrospective analysis of 1,103 SARS-CoV-2 wild-type-elicited mAbs shows that this method can increase the probability of identifying effective bnAbs to the XBB.1.5 strain from 1% to 40% in an early pandemic set-up. Among these bnAbs, BD55-1205 showed potent activity to all tested variants. Cryogenic electron microscopy structural analyses revealed the receptor mimicry of BD55-1205, explaining its broad reactivity. Delivery of mRNA–lipid nanoparticles encoding BD55-1205-IgG in mice resulted in serum half-maximal neutralizing antibody titre values of ~5,000 to XBB.1.5, HK.3.1 and JN.1 variants. Combining bnAb identification using viral evolution prediction with the versatility of mRNA delivery technology can enable rapid development of next-generation antibody-based countermeasures against SARS-CoV-2 and potentially other pathogens with pandemic potential.

Severe acute respiratory syndrome coronavirus 2 (SARS-CoV-2) continues to rapidly evolve to evade immunity induced by natural infection and vaccination, resulting in highly evasive variant lineages such as XBB.1.5 and JN.1 (refs. 1,2). These variants are continuously accumulating mutations at key receptor-binding domain (RBD) antigenic sites, such as L455, F456 and A475, which may substantially alter their antigenicity and further escape neutralizing antibodies (NAbs) elicited by repeated vaccination and infection[3–7].

Monoclonal NAbs targeting the SARS-CoV-2 RBD have shown high efficacy in the treatment and prevention of coronavirus disease 2019 (COVID-19), especially in high-risk individuals who do not mount robust immune responses to vaccination[8–12]. However, all previously approved anti-SARS-CoV-2 monoclonal antibodies (mAbs) and cocktail therapeutics, discovered before the emergence of variants of concern, have lost effectiveness to contemporary variants[13–16]. Since the emergence and rapid evolution of Omicron in 2021, numerous antibodies have been reported to be 'broadly neutralizing' or 'variant proof' based on their

A full list of affiliations appears at the end of the paper. ✉e-mail: xiangxi@ibp.ac.cn; laura.walker@modernatx.com; yunlongcao@pku.edu.cn

https://doi.org/10.1038/s41564-025-02030-7

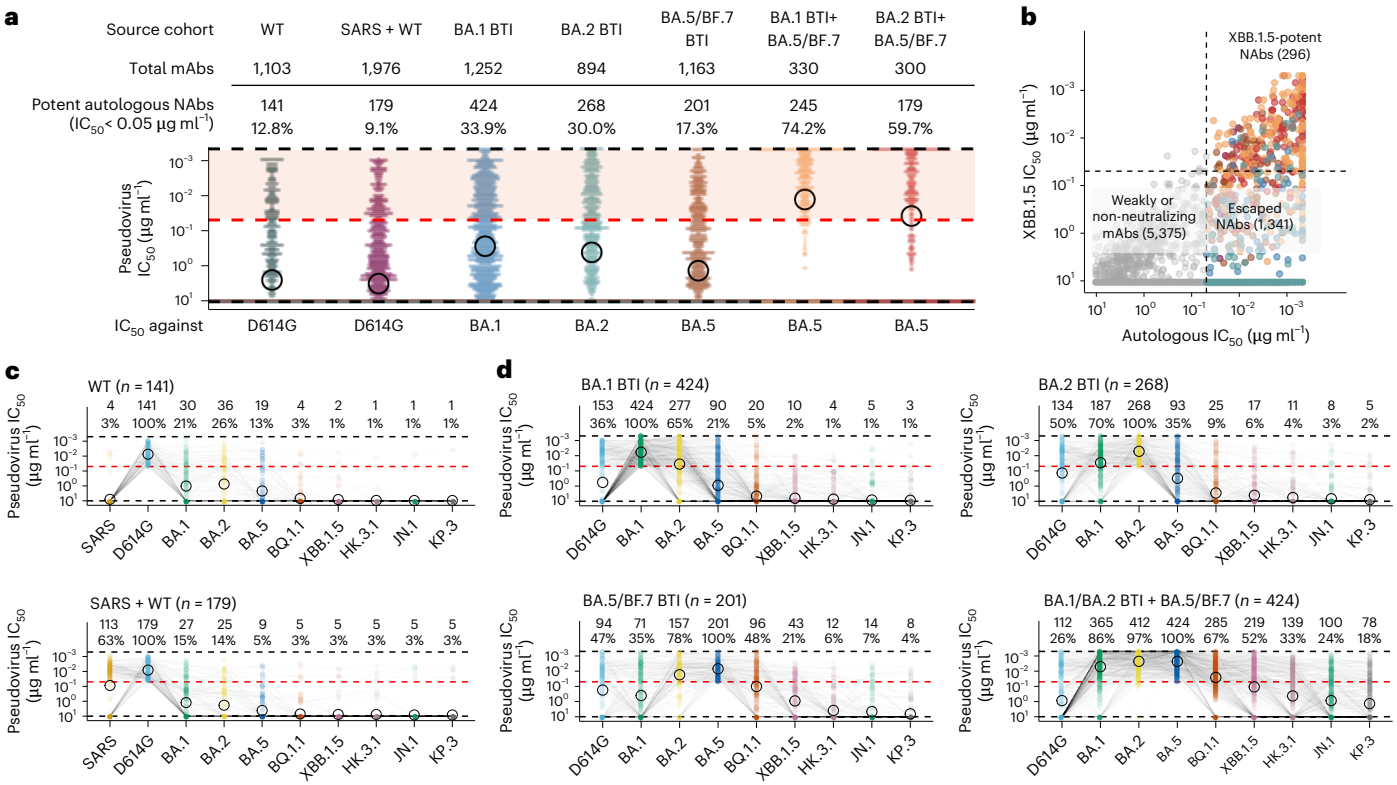

Fig. 1 | Neutralization activities of RBD-targeting mAbs to SARS-CoV-2 variants. a, Neutralization of the 7,018 mAbs from individuals with 7 different immune histories to the corresponding last-exposure variant (autologous neutralization activity). Numbers and proportions of potent autologous NAbs (IC_{50} < 0.05 μg ml^{-1}) are annotated above each group of points. The black circles indicate the geometric mean values of each group. The red dashed line (IC_{50} = 0.05 μg ml^{-1}) indicates the threshold for potent NAbs. The two black dashed lines indicate the upper and lower limit of detection (10 and 0.0005, respectively). **b**, Relationship between the autologous neutralization activities and XBB.1.5-neutralizing activities of the isolated mAbs. Different colours indicate antibodies from different cohorts (same as the colours in **a**). **c**,**d**, Neutralization activities of potent autologous NAbs from WT or SARS + WT cohort against SARS-CoV-1 and SARS-CoV-2 variants (**c**) and potent autologous NAbs from Omicron-exposed cohorts against SARS-CoV-2 variants (**d**). The numbers and proportions of potent NAbs to each variant (IC_{50} < 0.05 μg ml^{-1}) are annotated.

ability to neutralize historical SARS-CoV-2 variants, targeting either the RBD, amino-terminal domain or subdomain 1 of the virus spike glycoprotein[17–24]. Unfortunately, the vast majority of these antibodies rapidly lost activity to newly emerging variants, raising questions about the criteria used to designate antibodies as broadly neutralizing and undermining confidence in the development of next-generation antibodies to SARS-CoV-2 (refs. 14,25,26). Therefore, the development of a practical strategy to identify broadly neutralizing antibodies (bnAbs) with neutralizing activity to both existing and prospective variants would greatly enhance the feasibility of developing future antibody-based countermeasures to SARS-CoV-2 that can outpace viral evolution and would have been invaluable at the early stages of the pandemic.

Previously, we used high-throughput deep mutational scanning (DMS) on extensive panels of mAbs to characterize the evolutionary pressures on the SARS-CoV-2 RBD to predict future mutation hotspots[25,27]. Here we show that DMS-based mutation prediction can largely enhance the probability of identifying bnAbs that potently neutralize both existing and future variants. Using this method, we identified a human IGHV3-66-derived class 1 bnAb elicited by SARS-CoV-2 ancestral strain infection, designated as BD55-1205, which shows extraordinary neutralization breadth to all existing variants and prospective variants with mutations within its targeting epitope. Delivery of mRNA-encoded BD55-1205 IgG in mice resulted in a high serum neutralizing titre to evasive variants, providing evidence that mRNA technology could be leveraged for rapid deployment of anti-SARS-CoV-2 bnAbs. This platform may enable the rapid development of next-generation antibody-based countermeasures to SARS-CoV-2 and potentially future pandemic pathogens.

Results

Retrospective assessment of SARS-CoV-2 NAbs

To date, anti-SARS-CoV-2 NAbs that are potent to currently circulating variants have been selected for clinical development. However, such NAbs have been repeatedly evaded by Omicron variants, suggesting that activity against current variants does not translate into breadth against future variants[13,16,25]. To investigate the relationship between neutralization potency and breadth against SARS-CoV-2 variants, we studied a panel of 7,018 mAbs isolated from 7 previously described cohorts, which included individuals infected with or vaccinated for ancestral SARS-CoV-2 (hereafter denoted as wild type (WT)); individuals who experienced SARS-CoV-1 infection in 2003/2004 and received the 3-dose CoronaVac in 2021 (SARS+WT); convalescents who experienced BA.1, BA.2 or BA.5/BF.7 breakthrough infection (BTI) after 3-dose CoronaVac (BA.1 BTI, BA.2 BTI and BA.5/BF.7 BTI, respectively); and convalescents who experienced BA.1 or BA.2 BTI and were reinfected by BA.5 or BF.7 (BA.1 or BA.2 BTI+BA.5/BF.7)[13,14,25,27,28]. Of the 7,018 mAbs, we identified 1,637 potent autologous NAbs, defined as half-maximal inhibitory concentration (IC_{50}) < 0.05 μg ml^{-1}, to the corresponding last-exposure variant (Fig. 1a and Supplementary Table 1).

To systematically investigate the breadth of NAbs isolated from various cohorts, we tested the neutralization activities of the 1,637 potent autologous NAbs to 8 major SARS-CoV-2 variants, including B.1 (D614G), Omicron BA.1, BA.2, BA.5, BQ.1.1, XBB.1.5, HK.3 and JN.1

https://doi.org/10.1038/s41564-025-02030-7

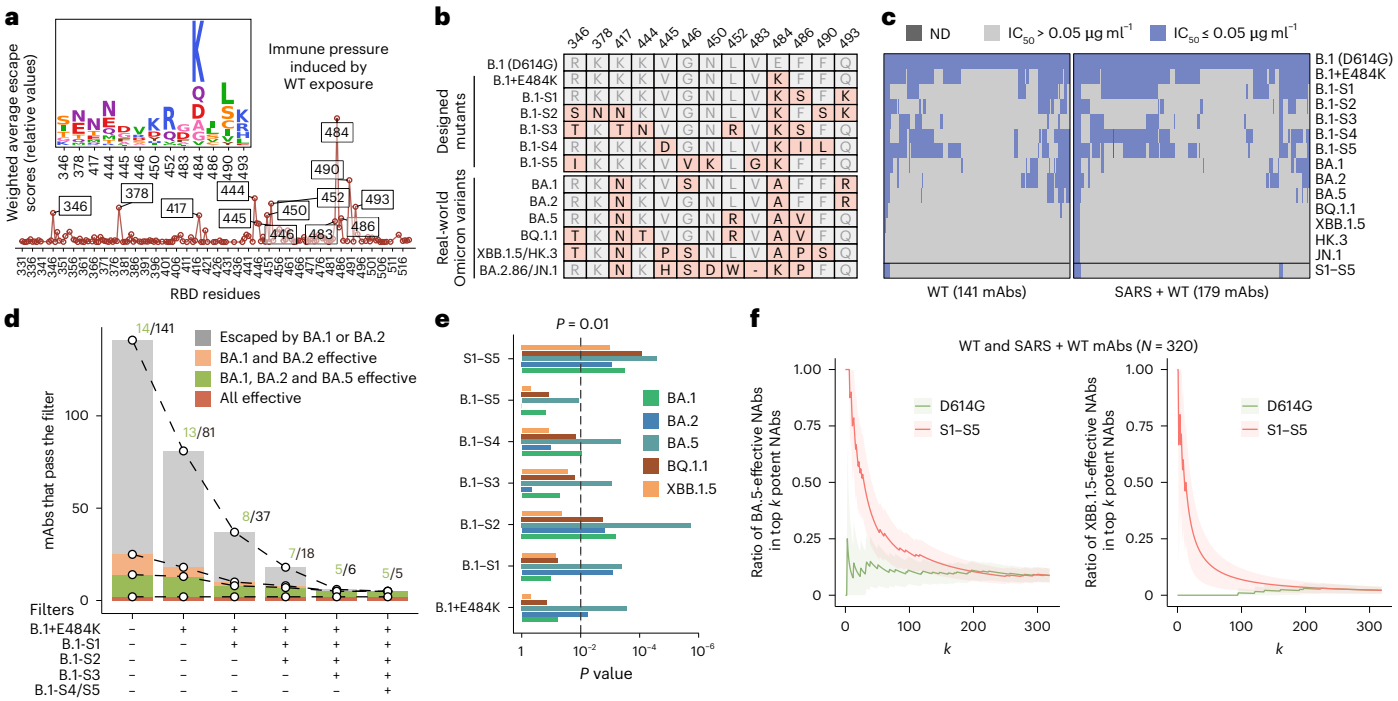

Fig. 2 | Designed mutants based on mutation prediction define bnAbs. **a**, Average escape profiles from DMS of mAbs (weighted by neutralization activities of each mAb to SARS-CoV-2 B.1 and the impact of each RBD mutation on ACE2 binding and RBD expression). The *y* axis corresponds to weighted average escape scores across all mAbs on each RBD residue (relative values). **b**, Mutations harboured by the designed SARS-CoV-2 B.1-based mutants and real-world variants on the key sites indicated by DMS-based prediction. The letters are standard one-letter code of amino acids. Coloured grids indicate the mutated residues compared to the B.1 strain. **c**, Neutralization capability of the mAbs from early cohorts (SARS+WT and WT) to the designed mutants and real-world Omicron variants. S1–S5 indicates the highest IC_{50} to the five designed mutants. **d**, Number of NAbs from WT vaccinees or convalescents that pass the filter of designed mutants. Ratios of BA.1-, BA.2- and BA.5-potent NAbs among the passed NAbs are annotated above the bar of each combination of filters. **e**, Significance for the enrichment of BA.1-, BA.2-, BA.5-, BQ.1.1- or XBB.1.5-potent NAbs within NAbs that are from WT vaccinees or convalescents and pass each filter of the designed mutants (two-sided hypergeometric test). **f**, Ratio of BA.5- or XBB.1.5-potent NAbs within the NAbs with the top '*k*' neutralization activities to D614G or S1–S5. *k* indicates the ranking, which ranges from 1 to the total number of mAbs. The error bars indicate 95% confidence intervals under normal distribution. ND, not determined.

(Fig. 1b–d). Among the 1,637 potent NAbs from 6 cohorts, only 296, 133 and 100 mAbs showed potent neutralization to XBB.1.5, JN.1 and KP.3, respectively (Fig. 1b and Extended Data Fig. 1a). Although there was an association between autologous and XBB.1.5, JN.1 or KP.3 neutralization activity, NAbs with the strongest autologous neutralization activities generally lost neutralization breadth to 'future' (at that time) variants; this phenomenon was particularly striking for NAbs obtained at the early stages of the pandemic from individuals infected or vaccinated with the ancestral strain (Fig. 1b and Extended Data Fig. 1b). Among the 141 WT-elicited potent NAbs, only 2 (1%) remained potent to XBB.1.5, and only 1 potently neutralized all tested variants including JN.1 (Fig. 1c). BA.1- and BA.2-elicited antibodies showed slightly better tolerance to subsequent Omicron subvariants, but nevertheless, only 10 of 424 (2%) and 17 of 268 (7%) showed activity to XBB.1.5, respectively (Fig. 1d). Although a higher proportion of mAbs from the BA.5/BF.7 BTI or reinfection cohorts neutralized BQ.1.1 and XBB.1.5, only 7% and 27%, respectively, potently neutralized JN.1 (Fig. 1d). The vast majority (85%) of SARS-CoV-1/SARS-CoV-2 cross-reactive mAbs isolated from the SARS+WT cohort showed abrogated activity to Omicron variants (Fig. 1c)[13,28]. Only 5 of the 179 autologous potent NAbs from SARS+WT potently neutralized all tested variants, and all of them belong to epitope group F3, similar to SA55 (ref. 28). Therefore, sarbecovirus-based identification of bnAbs does not guarantee neutralization breadth to emerging SARS-CoV-2 variants, and neutralization potency to circulating variants at the time of isolation is not a sufficient metric to define neutralization breadth. Thus, a generalizable strategy to accurately identify bnAbs that retain activity to future SARS-CoV-2 variants is of paramount importance for the development of next-generation NAb-based therapeutics.

The rational strategy to select bnAbs

Previously, we showed that the integration of DMS profiles accurately predicted positively selected mutations during viral evolution under humoral immune pressure[25,27]. We hypothesized that screening mAbs to pseudoviruses encoding predicted mutations could identify bnAbs resilient to future variants efficiently.

To validate this strategy, we retrospectively studied a collection of the mAbs elicited by SARS-CoV-2 WT exposure, which could be obtained early in the pandemic[29,30]. We integrated antibody DMS escape profiles, codon preferences, human ACE2 (hACE2) binding and RBD expression impacts to map hotspots on RBD, including R346, K378, K417, K444-G446, N450, L452, E484, F486, F490 and Q493 (Fig. 2a)[25,27,31]. We constructed 17 mutant pseudoviruses harbouring single amino acid substitutions at these positions based on the B.1 (D614G) strain (Extended Data Fig. 2a). As E484K is the most striking mutation from the calculation of hotspots based on DMS results, we first tested the neutralization activities of 141 potent NAbs from the WT cohort to B.1+E484K. For mAbs that remained effective, the neutralization activities to the other 16 single-substitution mutants were tested. These mutants can help enrich for Omicron-effective NAbs, increasing the frequency of BA.1-, BA.2- and BA.5-effective NAbs from 14 of 141 (9.9%) to 12 of 46 (26%) (Extended Data Fig. 2b). To enhance antibody escape, we further designed five mutants with a combination of these mutations, named B.1-S1 to B.1-S5 (Fig. 2b). The combinations were designed

https://doi.org/10.1038/s41564-025-02030-7

Table 1 | Characteristics of NAbs isolated from early cohorts that pass the designed filters

Antibody	Source	Epitope group	IGHV gene	Pseudovirus IC_{50} ($\mu g\,ml^{-1}$)													
				D614G	BA.1	BA.2	BA.5	BQ.1.1	XBB.1.5	HK.3.1	JN.1	KP.3	B.1+E484K	B.1-S1	B.1-S2	B.1-S3	B.1-S4	B.1-S5
BD-505	WT	A1	IGHV3-53	0.015	0.016	0.021	0.016	0.041	0.023	>10	>10	>10	0.011	0.032	0.028	0.010	0.033	0.016
BD55-1159	WT	A1	IGHV3-66	0.002	0.002	0.002	0.009	>10	>10	>10	>10	>10	0.004	0.004	0.017	0.006	0.008	0.005
BD55-1208	WT	A1	IGHV3-66	0.003	0.002	0.003	0.004	0.029	0.491	>10	>10	>10	0.013	0.006	0.024	0.033	0.011	0.007
BD55-279	WT	A1	IGHV3-53	0.014	0.004	0.001	0.006	0.227	0.228	>10	>10	>10	0.003	0.009	0.026	0.003	0.008	0.004
BD55-1205	WT	A1	IGHV3-66	0.003	0.005	0.006	0.003	0.009	0.006	0.012	0.008	0.004	0.002	0.006	0.011	0.006	0.003	0.004
BD55-5713	SARS	F3	IGHV2-5	0.006	>10	>10	>10	>10	>10	>10	>10	>10	0.005	0.011	0.010	0.032	0.031	0.024
BD55-6723	SARS	E1	IGHV2-26	0.005	0.186	0.151	0.279	0.289	>10	>10	>10	>10	0.008	0.011	0.003	0.041	0.005	0.020
BD55-5286	SARS	E1	IGHV7-4-1	0.001	0.093	0.057	0.108	>10	>10	>10	>10	>10	0.002	0.034	0.002	0.010	0.011	0.011
BD55-5484	SARS	E1	IGHV7-4-1	0.001	0.003	0.011	0.013	>10	>10	>10	>10	>10	0.001	0.012	0.002	0.025	0.008	0.041
BD55-3372	SARS	F3	IGHV3-21	0.007	0.020	0.032	0.015	0.023	0.019	0.038	0.032	0.025	0.010	0.006	0.027	0.008	0.015	0.021
BD55-4637	SARS	F3	IGHV2-5	0.020	0.023	0.023	0.024	0.019	0.023	0.043	0.017	0.030	0.023	0.033	0.043	0.021	0.018	0.022
BD55-5300	SARS	F3	IGHV1-69	0.005	0.008	0.007	0.005	0.030	0.021	0.032	0.004	0.004	0.011	0.029	0.012	0.021	0.022	0.017
BD55-5483	SARS	F3	IGHV1-69	0.014	0.006	0.013	0.004	0.003	0.007	0.008	0.008	0.009	0.014	0.007	0.016	0.019	0.007	0.007
SA55	SARS	F3	IGHV1-69	0.011	0.002	0.007	0.005	0.005	0.006	0.012	0.006	0.007	0.004	0.010	0.005	0.009	0.006	0.006

to maintain hACE2 binding and avoid multiple mutations in the same epitope (Supplementary Information). As expected, these mutants, especially B.1-S3 (R346T+K417T+K444N+L452R+E484K+F486S), substantially escaped the majority of potent NAbs elicited by WT exposure (Fig. 2c and Extended Data Fig. 2a). Passing the filter of all five design mutants (S1–S5 refers to the weakest neutralization to the five designed mutants) is shown to be an efficient indicator of broad neutralization to real-world Omicron variants (Fig. 2d,e). NAbs potently neutralizing all the B.1-S1 to B.1-S5 mutants significantly enriches true bnAbs capable of neutralizing Omicron subvariants (Fig. 2e).

Only 5 of 141 NAbs from WT remained potent (IC_{50} < 0.05 μg ml^{-1}) to all the rationally designed evasive mutants (Fig. 2d). Notably, although the mutations of our predicted mutant sequences only partially overlap with real-world Omicron variants, all five NAbs with activity against all rationally designed mutants effectively neutralized Omicron BA.1, BA.2 and BA.5. Importantly, the five selected bnAbs include the only two XBB.1.5-effective antibodies among the whole collection of 141 candidates, which corresponds to an increase in the probability of identifying 'true' bnAbs from ~1% to 40%. Overall, our model correctly predicted the key escape mutations incorporated during SARS-CoV-2 antigenic drift and allowed for the identification of a small subset of WT-elicited bnAbs with activity against future variants.

In addition, we analysed the panel of 320 NAbs from WT (n = 141) and SARS+WT (n = 179) cohorts, all of which could have been obtained early in the pandemic. Similarly, the neutralization activities of the SARS+WT-elicited NAbs to the designed mutants predicted BA.5/XBB.1.5 activity (Extended Data Fig. 2b,c). In contrast, most potent B.1 NAbs were evaded by XBB.1.5/JN.1, underscoring the value of designed mutants (Fig. 2f and Extended Data Fig. 2d,e). The results validate our viral evolution prediction platform for the identification of rare, resilient bnAbs from a large collection of antibodies isolated from individuals who were convalescent or vaccinated at the early stage of a pandemic.

BD55-1205 shows a high barrier to escape

BD55-1205, a class 1 public antibody that uses the IGHV3-53/3-66 germline[29,32,33], was the only JN.1-effective bnAb from the WT cohort (Table 1). It shows the strongest S1–S5 neutralization (referring to the weakest in five designs), which may reflect its better tolerance to mutations compared with other competitors in epitope group A1. Given that BD55-1205 showed broad neutralization to all variants tested, we assessed whether it also showed a high barrier to escape under stringent in vitro conditions. Using XBB.1.5 S-pseudotyped replication-competent recombinant vesicular stomatitis virus (rVSV), we screened for antibody escape mutations via serial passage in Vero cells (Fig. 3a and Extended Data Fig. 3a)[34,35]. This assay simulated the viral evolution under the pressure of a specific mAb. For comparison, a bnAb SA55 and a non-competing pair of XBB.1.5-effective bnAbs (BD57-1520+BD57-2225) were included (Extended Data Fig. 3b–d)[27]. Surprisingly, BD55-1205 showed similar resistance to viral escape as the bnAb cocktail, retaining neutralization until passage 6 (Fig. 3b and Extended Data Fig. 4d,e). In contrast, individual SA55, BD57-2225 or BD57-1520 antibodies were evaded after two or three passages (Fig. 3b and Extended Data Fig. 4a–c). Substitutions L455P, Q493R/K, N417K, A435T and D420Y were enriched in the BD55-1205-selected virus, consistent with critical residues interacting with class 1 antibodies, as indicated by DMS based on the BA.5 or XBB.1.5 RBD (Fig. 3c and Extended Data Fig. 3c,d). To validate the selected mutations, we constructed XBB.1.5+L455P+Q493R, XBB.1.5+N417K+A435T and XBB.1.5+D420Y+Q493K mutant pseudoviruses. The activity of BD55-1205 against these pseudoviruses is reduced but not completely evaded (Fig. 3d). Neutralization assays using soluble hACE2 indicated a lower receptor-binding capability of these mutants compared with XBB.1.5 (Fig. 3d and Extended Data Fig. 5a,b), suggesting that the mutations abrogating BD55-1205 activity may result in reduced viral fitness through disruption of receptor-binding interactions.

We then evaluated neutralization to new real-world and prospective variants, including XBB-, BA.2.86- or JN.1-derived subvariants with mutations on L455, F456, A475 and Q493 (critical sites targeted by class 1 antibodies)[27,36]. BD55-1205 remains potent, whereas many other class 1 NAbs are evaded by JN.1+F456L and KP.3 (Fig. 3d). Surprisingly, the neutralization of BD55-1205 to KP.3 is even stronger than that to JN.1 and JN.1+F456L, consistent with the stronger ACE2-binding of KP.3 due to F456L-Q493E epistasis, which further underscores the ACE2 mimicry[36,37]. BD55-1205 IgG showed high apparent affinity to variant RBDs, ranging from 1 pM to 18 nM, in line with its exceptional tolerance to mutations on the epitope (Extended Data Fig. 5c,d).

BD55-1205 also potently inhibited authentic SARS-CoV-2 WT, BA.5.2.1, FL.8, XBB.1.5.6 and JN.3 isolates with IC_{50} values from 0.007 μg ml^{-1} to 0.026 μg ml^{-1} (Extended Data Fig. 6a). Escape mutation selection with XBB.1.5.6 authentic virus revealed no notable escape in some assay wells even after 12 passages (Extended Data Fig. 6b), and deep sequencing identified only 1 mutation within the BD55-1205 epitope, S490Y (Extended Data Fig. 6c). However, the neutralization activity of BD55-1205 is only slighted reduced against XBB.1.5+S490Y pseudovirus compared with XBB.1.5 (Extended Data Fig. 6d). Interestingly, the ACE2 inhibition efficiency to XBB.1.5+S490Y is also dampened, again highlighting ACE2-mimicking binding (Extended Data Fig. 6e). Only eight SARS-CoV-2 sequences with 490Y have been observed from 22 January 2024 to 19 July 2024 (https://cov-spectrum.org), indicating low real-world prevalence.

Structural analyses of BD55-1205

To elucidate the structural basis of BD55-1205's exceptional breadth, we determined the structure of XBB.1.5 S ectodomain trimer in complex with the BD55-1205 antigen-binding fragment (Fab) using cryogenic electron microscopy (cryo-EM) (Extended Data Fig. 7a). We asymmetrically reconstructed the complex structure at an overall resolution of 3.5 Å, with 1 conformational state referred to as the 3 'open' RBDs observed (Extended Data Fig. 8a). The high flexibility of three open RBDs complicates the alignment during data processing, hence limiting the resolution of the interface in the XBB.1.5 S–BD55-1205 complex. Consequently, we determined the cryo-EM structure of the XBB.1.5 RBD in complex with BD55-1205 Fab (Extended Data Fig. 7b) to further investigate the antibody–RBD interface. The structure of the RBD is similar to a published model from crystallography (Extended Data Fig. 8d).

Consistent with DMS, BD55-1205 is a class 1 antibody that binds to the apical head of RBD, partially overlapping the receptor-binding motif and RBD core (Fig. 4a)[38]. BD55-1205 has a relatively short complementarity-determining region (CDR) H3 of 11 amino acids (IMGT convention) compared with the average in the unselected repertoire[39,40]. The antibody footprint on RBD shows substantial overlap with the hACE2 receptor-binding sites (Fig. 4b and Extended Data Fig. 8b). The distal tip of the receptor-binding motif deeply inserts into a cavity formed by 5 CDRs—light chain (LC) CDR1 and CDR3 and heavy chain (HC) CDR1–3—resulting in ~1,100 Å^2 buried area via LC (30%) and HC (70%) contributions (Extended Data Fig. 8c). The epitope of BD55-1205 encompasses over 20 residues, forming an extensive patch along the receptor-binding ridge (Extended Data Fig. 8g). Binding of RBD to BD55-1205 is primarily mediated by polar interactions, many of which involve contacts with the RBD carbon backbone. A total of 17 hydrogen bonds are formed between the side chains of RBD and CDR residues, involving R403, N405, T415, N417, D420, N487, Y489, Q493, Y501 and H505 on the RBD; Y33, S56, R97, R102 and E104 on the HC-CDR (HCDR); and N30 and D93 on the LC-CDR (LCDR) (Fig. 4c). In addition, 12 hydrogen bonds are formed between the backbone atoms of 9 RBD residues (L455, R457, K458, Q474, A475, G476, S490, L492 and G502), HCDR (T28, R31, N32, Y33, P53 and R102) and LCDR (S28) (Fig. 4d–g and Extended Data Figs. 8e,f and 9a). Furthermore, a network of hydrophobic interactions also contributes to the RBD–BD55-1205 interactions, involving G416, Y453, L455 and F456 from

https://doi.org/10.1038/s41564-025-02030-7

a

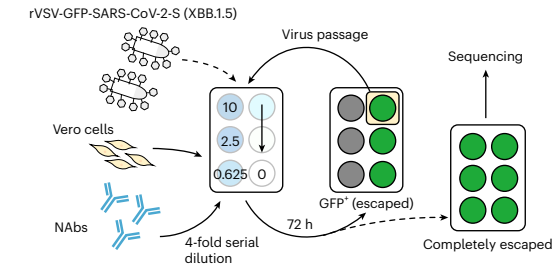

b

Antibody	Repeat	P1	P2	P3	P4	P5	P6	P7	P8	P9	P10	Mutations
BD55-1205	1	0.039	0.156	0.625	0.625	0.625	10					L455P+Q493R
	2	0.039	0.156	0.625	0.625	0.625	2.5	2.5	10			N417K, A435T
	3	0.039	0.156	0.625	0.625	0.625	2.5	0.625	10			D420Y, Q493K
SA55	1	0.156	10									G504S/D
	2	0.156	10									
BD57-2225 +1520	1	0.156	0.156	0.156	0.156	2.5						K478E, T500K
	2	0.156	0.156	0.156	0.156	0.156	0.156	0.156	0.156	0.625	2.5	F371I, K440E, K478Q,T500A
	3	0.156	0.156	0.156	0.156	0.625	2.5					A475V, T500K
BD57-2225	1	0.039	0.625	2.5								K478E, N487D
	2	0.039	0.625	2.5								K478E, N487D/K
	3	0.039	0.625	2.5								N487D
BD57-1520	1	0.156	10									T500K/A
	2	0.156	10									T500K
	3	0.156	10									N450D, T500K

c

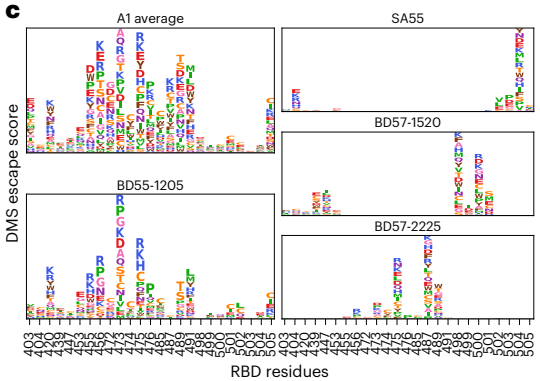

d

IC_{50} (μg ml^{-1})		Indicated by rVSV screening or DMS			Prospective escape mutants								
	XBB.1.5	XBB.1.5 +L455P+ Q493R	XBB.1.5 +N417K +A435T	XBB.1.5 +D420Y +Q493K	HK.3.1	JN.1	JN.1 +F456L	KP.3	BA.2.86 +FLip +A475V	JN.1 +F456L +A475V	JN.1.23 +D420N	JN.1.23 +Y489H	JN.1.23 +F456L+ A475V
Soluble hACE2	0.17	1.1	5.6	0.29	0.03	0.07	0.08	0.03	0.08	0.19	0.07	0.24	0.15
BD55-1205	0.006	2.353	0.549	0.182	0.012	0.008	0.012	0.004	0.013	0.021	0.005	0.030	0.033
BD56-1854	0.001	0.094	0.266	0.024	0.004	0.002	0.051	0.043	>10	>10	4.831	0.261	>10
BD57-0309	0.010	>10	1.911	>10	0.008	0.006	1.479	>10	>10	>10	>10	>10	>10
BD57-0968	0.010	0.120	0.816	0.066	0.032	0.021	0.015	0.025	0.051	>10	0.406	0.051	>10
BD57-1519	0.019	0.642	0.386	0.105	0.007	0.008	0.109	0.208	>10	>10	2.652	>10	>10
BD57-1547	0.006	0.096	>10	0.009	0.011	0.041	>10	>10	>10	>10	>10	>10	>10
BD57-2578	0.005	>10	0.457	0.503	0.014	0.011	0.013	1.080	0.005	0.957	>10	0.296	>10
BD57-2587	0.006	0.423	0.191	0.800	0.012	0.010	0.243	>10	0.086	>10	>10	>10	>10
BD57-2225	0.001	0.001	0.007	0.001	0.101	0.001	0.004	0.011	>10	1.316	0.002	0.032	1.192
BD57-1520	0.002	0.030	0.064	0.003	0.006	0.006	0.009	0.003	0.004	0.007	0.004	0.006	0.003

Fig. 3 | BD55-1205 shows extraordinary resistance to viral escape. a, Schematic for the rVSV-based escape mutation screening assays. **b**, Results of the escape mutant screening by passaging rVSV under NAb pressure. Values in the P1–P10 columns of the table indicate the highest concentration (μg ml^{-1}) of NAb that was evaded by rVSV in the first passage to the tenth passage. The mutations observed in the final passage of rVSV were determined by Sanger sequencing and are annotated in the last column. The coloured grid highlights the rVSV passages that strongly escape the antibody (concentration ≥ 2.5 μg ml^{-1}). **c**, DMS escape profiles (based on XBB.1.5 RBD) of the NAbs evaluated in the rVSV assays. The average profile of antibodies in epitope group A1 is also shown for comparison with BD55-1205. **d**, Neutralization of BD55-1205 and other NAbs to designed escape mutants identified by rVSV screening and DMS profiles, and to real-world emerging and prospective mutants with mutations in the BD55-1205 epitope. BD57-2225 and BD57-1520 are bnAbs targeting different epitopes and included for comparison.

XBB.1.5 RBD; Y33, Y52, F58, L99 and I101 from the HC; and W94 and P95 from the LC (Fig. 4h). We compared BD55-1205's interactions with other published class 1 NAbs that show some extent of neutralization breadth, including P5S-1H1, P5S-2B10, BD-604 and Omi-42 (Fig. 4i,j and Extended Data Fig. 9a–c)[32,41,42]. Omi-42 is susceptible to A475V and L455F+F456L mutations emergent in several XBB.1.5 and BA.2.86 lineages (Fig. 4i)[4]. The recognition of P5S-2B10 and P5S-1H1 is affected by N460K, which abrogates the hydrogen bonds on their interfaces (Fig. 4j). However, the extensive interactions with the RBD backbone confer BD55-1205's broad and resilient reactivity (Extended Data Fig. 9a). Despite the unaffected neutralization activity, L455S and A475V moderately dampen the affinity of BD55-1205 to RBD (Extended Data Fig. 5c). This could be explained by the potential impacts on the hydrophobic interactions involving L455 and by a hydrogen bond between HC N32 and A475 backbone (Fig. 4h,i). Compared with the other IGHV3-53- or IGHV3-66-derived NAbs (P5S-2B10, P5S-1H1 and BD-604), BD55-1205 has three unique residues in its HCDRs that were introduced by somatic hypermutation or V(D)J recombination and make contacts with the RBD backbone atoms: R31 on HCDR1, P53 on HCDR2 and R102 on HCDR3 (Extended Data Fig. 9b). These mutations, especially R31 and R102, introduce additional polar interactions at the interface (Fig. 4k). Mutants of BD55-1205 carrying the R31S, P53S or R102Y substitutions and the IGHV germline-reverted version (BD55-1205-GLHV) with the mature HCDR3 retained neutralization to BA.5, HK.3.1, JN.1 and JN.1+F456L. However, BD55-1205-GLHV lost neutralizing activity to JN.1+F456L+A475V (Extended Data Fig. 9d), and the apparent affinity of BD55-1205-GLHV to WT, BA.5, XBB.1.5, HK.3 and JN.1 RBD showed a substantial decrease (Extended Data Fig. 9e). These findings show that these unique mutations only partially explain BD55-1205's superior breadth, indicating that the 11-aa HCDR3 is probably the major determinant of the broad reactivity. Nevertheless, these IGHV somatic hypermutations enhance its RBD-binding affinity and potentially increase its ability to withstand further antigenic variation.

bnABs encoded by mRNA–lipid nanoparticles yield high serum neutralizing titre

Recombinant mAbs or antibody cocktails have been shown to be clinically active in the prevention of symptomatic COVID-19 (refs. 8–10,43). Alternative means for delivery of therapeutic antibodies to patients—to the current standard of recombinant mAb products—could prove advantageous towards more rapid and widespread deployment in a pandemic or epidemic context. To that end, we encoded BD55-1205 in mRNA and formulated it into lipid nanoparticles (LNPs) for in vivo delivery, similar to mRNA vaccines (Methods). We introduced the 'LA' modification (M428L/N434A) in the crystallizable fragment (Fc) region to enhance human neonatal Fc receptor (FcRn) binding at an acidic pH, thereby improving the antibody half-life[44]. Formulated LNPs were delivered by intravenous injection to Tg32-SCID transgenic female mice that were homozygous for human FcRn[45]. To assess BD55-1205 IgG expression kinetics, we quantified human IgG concentration in mouse sera collected at the indicated time intervals after mRNA-LNP delivery via enzyme-linked immunosorbent assay (ELISA) (Fig. 5a). We previously reported on in vivo pharmacokinetics of the mRNA-encoded chikungunya virus E2 glycoprotein-specific antibody CHKV-24 (mRNA-1944) determined in a phase 1 clinical trial[46,47]. CHKV-24, with a human half-life of 69 days, was used here as an expression and half-life benchmark, and it showed expression kinetics that were highly similar to BD55-1205 in the Tg32-SCID mouse (Fig. 5b)[46]. At 48 h, serum antibody levels peaked at 505 μg ml^{-1} and 491 μg ml^{-1} for BD55-1205 and CHKV-24, respectively (Fig. 5c). Given that serum neutralizing titres are an established correlate of protection from SARS-CoV-2

https://doi.org/10.1038/s41564-025-02030-7

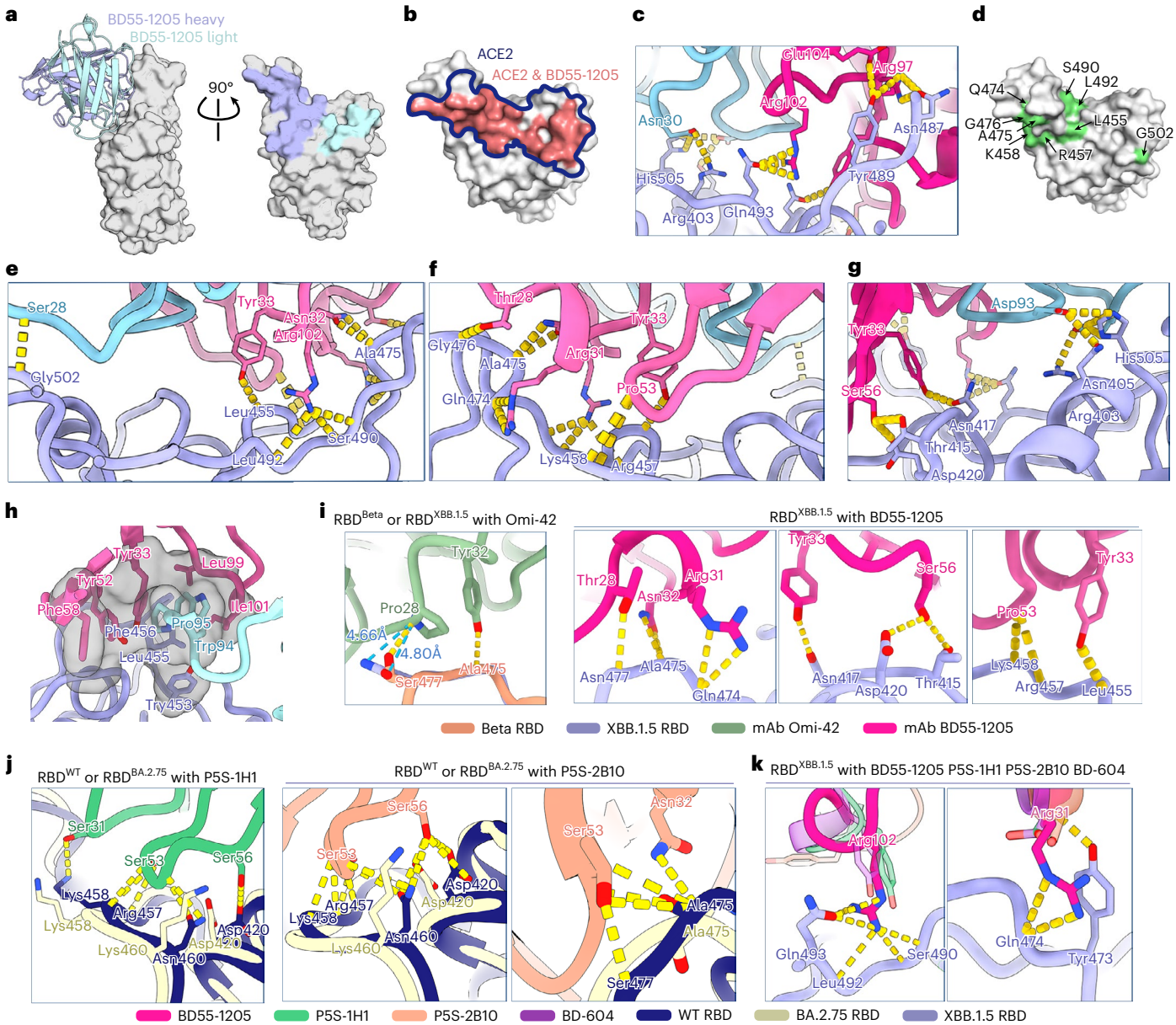

Fig. 4 | Structural basis for the broad reactivity of BD55-1205. a, Structural model of SARS-CoV-2 XBB.1.5 RBD in complex with BD55-1205 from cryo-EM data. **b**, Overlay of BD55-1205 and hACE2 binding footprints on XBB.1.5 RBD. **c**, Polar interactions between BD55-1205 and XBB.1.5 RBD side chain atoms. **d**, RBD backbone interactions with BD55-1205 Fab. **e**–**g**, Polar interactions between BD55-1205 HC or LC and XBB.1.5 RBD backbone atoms in the binding interface mediated by HCDR3 (**e**), HCDR1/2 (**f**) and LCDR3 (**g**). Yellow dashed lines indicate potential polar interactions. RBD, HC and LC are coloured in blue, magenta and cyan, respectively. **h**, Hydrophobic interaction between RBD and BD55-1205. **i**–**k**, Comparison of the RBD interactions with BD55-1205 and other class 1 NAbs, including Omi-42 (**i**), P5S-1H1 and P5S-2B10 (**j**), BD-604 (**k**) (PDB: Omi-42, 7ZR7; P5S-1H1, 7XS8; P5S-2B10, 7XSC; BD-604, 8HWT).

(refs. 43,44,48,49), we also evaluated the neutralizing titre to XBB.1.5, HK.3.1 and JN.1 pseudoviruses. BD55-1205 achieved a high geometric mean peak serum half-maximal inhibitory dilution (ID_{50}) of 4,496 to XBB.1.5, 5,138 to HK.3.1 and 4,608 to JN.1 at 48 h post-administration, underscoring the antibody's breadth (Fig. 5d,e). As expected, we observed a significant correlation between serum IgG concentrations and ID_{50} to the three variants (Fig. 5f). mRNA-LNP delivery of BD55-1205 to immunocompetent Tg32 mice showed similar peak serum concentrations in both female and male mice (Extended Data Fig. 10a–c). Altogether, we show that a high serum antibody titre can be achieved after mRNA delivery in a mouse model. The speed and flexibility of mRNA-LNP delivery, coupled with our bnAb prediction methodology, could accelerate the development and deployment of next-generation antibody therapeutics to SARS-CoV-2.

Discussion

In this study, we analysed a large collection of RBD-targeting mAbs from individuals with diverse SARS-CoV-2 exposure histories to show the feasibility of high-throughput DMS for accurate and rational variant prediction. This led to the identification of BD55-1205, a class 1 bnAb derived from IGHV3-66 in a WT-exposed donor, which neutralized all major variants. Although discovered in early 2021, the broad neutralization of BD55-1205 was not appreciated until the emergence of XBB variants in 2023. This underscores the need for rapid identification of such bnAbs and highlights the potential of our prediction framework to facilitate the development of durable antibody drugs early in a pandemic.

Previously, we proposed selecting NAbs targeting immunorecessive epitopes to minimize selection pressure from herd immunity or

https://doi.org/10.1038/s41564-025-02030-7

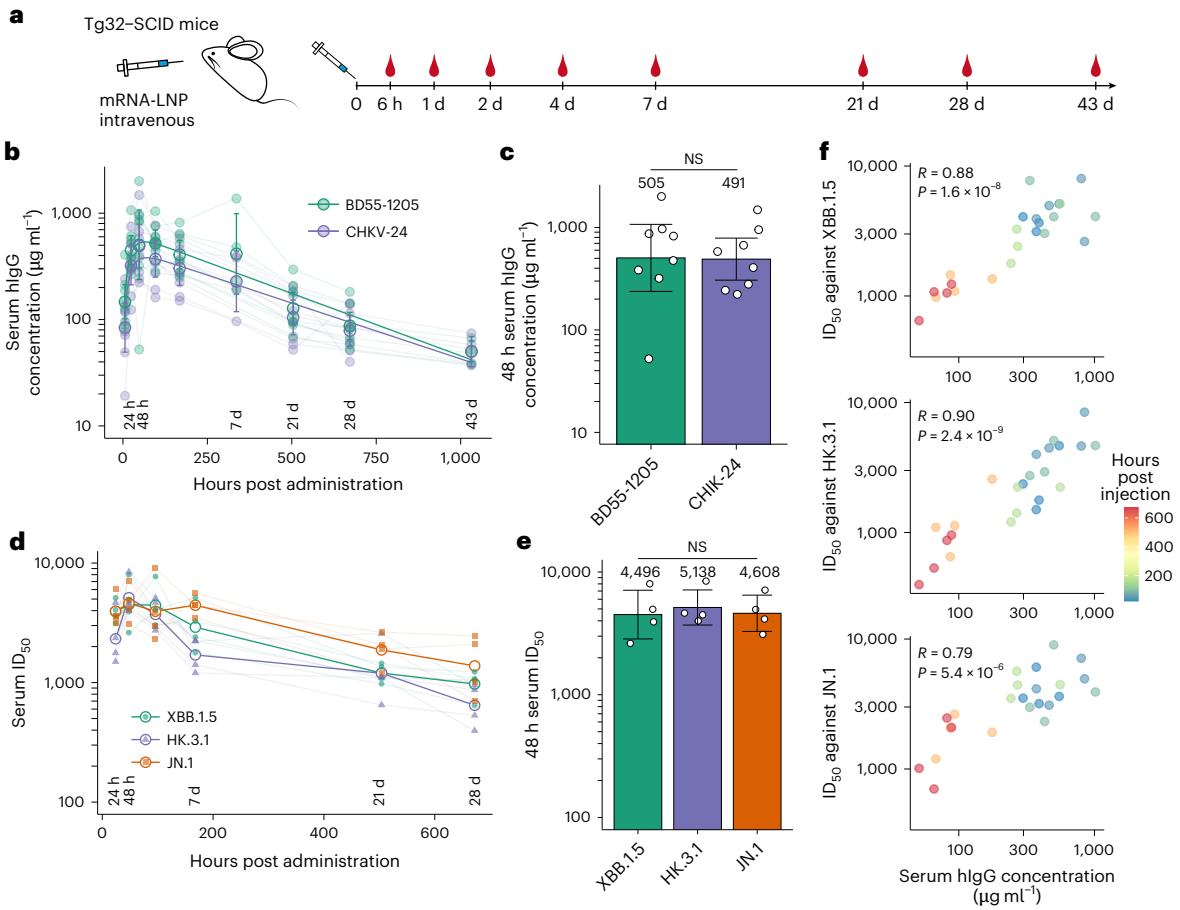

Fig. 5 | mRNA delivery of BD55-1205 in mice. a, A schematic of the experimental design for delivery of BD55-1205 and CHKV-24 via LNP-encapsulated mRNA in Tg32-SCID mice. Female mice, 4 per group, received a 0.5 mg kg^{-1} dose by intravenous injection on day 0 and serum was collected at the indicated time points. **b**, Serum concentration of BD55-1205 and a benchmark antibody CHKV-24 plotted over time. The geometric mean with error (95% confidence interval) is shown by outlined circles with error bars; solid symbols indicate individual animals. A biexponential curve was fitted to the data. Two independent in vivo experiments were combined, each with $n = 4$ animals per group. **c**, Peak serum concentration, occurring at 48 h after LNP administration, for BD55-1205 ($n = 8$, the 2 groups are merged) and CHKV-24 ($n = 4$). The bar height and the number above the bar indicate the geometric mean, error bars indicate 95% confidence intervals and empty symbols indicate individual animals. NS indicates non-significance (two-sided Wilcoxon rank-sum test). **d**, ID_{50} values of the mouse sera to XBB.1.5, HK.3.1 and JN.1 VSV pseudoviruses for BD55-1205 plotted over time. The geometric mean values are shown as the coloured empty circles and lines. The ID_{50} values for individual mouse serum samples are shown as coloured points and lines. **e**, Peak serum neutralizing titre in mice receiving BD55-1205 mRNA ($n = 4$, only 1 group was tested for neutralization) to the 3 indicated viral variants. The bar height and the number above the bar indicate the geometric mean, error bars indicate the 95% confidence interval and empty symbols indicate individual animals. NS indicates non-significance (two-sided Wilcoxon rank-sum test applied to any pair of variants). **f**, Scatter plots showing the correlation between serum hIgG concentrations and the ID_{50} to the three variants at indicated time points. Pearson correlation coefficients (R) and the corresponding significance P values are annotated (two-sided t-test).

public Ab responses[28]. However, this may not apply to newly emergent pathogens or early-pandemic scenarios when epitope immunodominance is unclear. Here we show that true bnAbs need not exclusively target 'rare' epitopes but rather require contacts that can accommodate future mutations. BD55-1205 can withstand high epitope variability over time owing to its high affinity, receptor mimicry and a binding mode that uses interactions with RBD backbone atoms. Our study defines key molecular criteria and a platform capable of identifying bnAbs such as BD55-1205 in several months, with potential activity retention for multiple years post-discovery.

This rapid bnAb identification process can synergize with the advantages of mRNA-LNP delivery of antibodies. Here, and in previous studies, we showed that high peak serum antibody concentrations and neutralizing titre can be achieved with mRNA delivery[46]. BD55-1205 delivered in mice reached serum levels surpassing CHKV-24, which previously achieved protective levels in clinical trials. Furthermore, the mRNA-LNP platform offers several advantages: (1) rapid product updates during a pandemic, (2) the ability to deliver alternative isotypes such as IgA for enhanced mucosal protection[50], (3) co-delivery of multiple antibodies to broaden protection to single or multiple pathogens, and (4) compatibility with multispecific antibodies engineered for superior breadth and potency. This opens up the potential of passive immunotherapy beyond what is possible with conventional antibodies and recombinant antibody delivery.

Although the approach described here offers a promising path to the identification of resilient anti-SARS-CoV-2 mAb therapeutics, it may be constrained by several practical limitations, including (1) the development of a robust DMS system for new pathogens, which may be challenging for some viruses; (2) the lack of established assays to predict efficacy; (3) insufficient samples for mAb screening; and (4) unpredictable viral saltations or epistasis beyond the current DMS scope.

Altogether, the accurate viral evolution prediction and mRNA–mAb delivery platform described here provide a practical framework for the rapid identification and deployment of bnAbs to combat future SARS-CoV-2 variants. We also envision that this platform could be

adapted to respond to other known pathogens with high pandemic potential, such as influenza, or even new viruses associated with 'Disease X' in the future.

Methods

Ethics statement

Use of authentic SARS-CoV-2 virus strains was undertaken with the approval of the Institutional Biosafety Committee of the Beijing Key Laboratory for Animal Models of Emerging and Remerging Infectious Diseases (application number GH2004), and studies were conducted in a biosafety level 3 facility. All animal studies were conducted under an Institutional Animal Care and Use Committee (IACUC)-approved protocol (IACUC 23-07-016) in compliance with the Animal Welfare Act, Public Health Service policy, and other applicable state and city public laws and regulations. Animal studies are designed and executed following the guidelines from the Guide for the Care and Use of Laboratory Animals, 8th Edition.

Cell culture

For the viral escape assay, African green monkey kidney Vero E6 cells (CRL-1586/VERO C1008; American Type Culture Collection (ATCC)) were maintained in Dulbecco's Modified Eagle's Medium (DMEM) high glucose (Euroclone) supplemented with 2 mM L-glutamine (Euroclone), 100 units ml^{-1} of penicillin–streptomycin (Gibco, Life Technologies) (complete DMEM medium) and 10% fetal bovine serum (FBS; Euroclone).

For the plaque reduction neutralization test (PRNT), Vero E6 cells were maintained in MEM (Gibco, Life Technologies) supplemented with 2 mM L-glutamine, 100 units ml^{-1} of penicillin–streptomycin, non-essential amino acids (Gibco, Life Technologies), 25 mM HEPES (Gibco, Life Technologies) and 10% FBS (PRNT MEM). Cells were incubated at 37 °C in a humidified atmosphere with 5% CO_2 and passaged every 3–4 days.

Antibody expression and purification

Antibody HC and LC genes were codon optimized and synthesized by GenScript, then separately inserted into vector plasmids (pCMV3-CH, pCMV3-CL or pCMV3-CK) via infusion (Vazyme). All antibodies were constructed with the human IgG1 constant region. The plasmids were co-transfected into Expi293F cells (A14527; Thermo Fisher) using polyethylenimine transfection. The transfected cells were cultured at 36.5 °C in 5% CO_2 for 6–10 days. The expression fluid was collected and centrifuged, and then supernatants containing mAbs were purified by Protein A Magnetic Beads (L00695-20; GenScript). The purified mAb samples were verified by SDS–PAGE (P42015; Lablead Biological).

Pseudovirus design and neutralization assays

We identified the escape hotspots in SARS-CoV-2 WT exposure cohorts as described previously[25]. In brief, DMS escape scores of each WT-elicited mAb and each RBD mutation were averaged, weighted by the pseudovirus IC_{50} of each mAb to SARS-CoV-2 D614G and the impacts on ACE2 binding and RBD expression indicated by DMS[31].

The SARS-CoV-2 WT spike glycoprotein sequence was from the reference genome (MN908947). Spike-pseudotyped viruses of SARS-CoV-2 variants were prepared based on a VSV pseudovirus packaging system as described previously[51]. Briefly, the spike plasmid of each variant was cloned into the pcDNA3.1 vector (BA.1, A67V+H69–V70del+T95I+G142D+V143–Y145del+N211del+L212I+R214–D215insEPE+G339D+S371L+S373P+S375F+K417N+N440K+G446S+S477N+T478K+E484A+Q493R+G496S+Q498R+N501Y+Y505H+T547K+D614G+H655Y+N679K+P681H+N764K+D796Y+N856K+Q954H+N969K+L981F; BA.2, T19I+L24–P26del+A27S+G142D+V213G+G339D+S371F+S373P+S375F+T376A+D405N+R408S+K417N+N440K+S477N+T478K+E484A+Q493R+Q498R+N501Y+Y505H+D614G+H655Y+N679K+P681H+N764K+D796Y+Q954H+N969K; BA.5, BA.2+H69–V70del+L452R+F486V+R493Q; BQ.1.1, BA.5+R346T+K444T+N460K; XBB.1.5, BA.2+V83A+Y144del+H146Q+Q183E+V213E+G339H+R346T+L368I+V445P+G446S+N460K+F486P+F490S+R493Q; HK.3, XBB.1.5+Q52H+L455F+F456L; JN.1, BA.2+V16–N17insMPLF+R21T+S50L+H69–V70del+V127F+Y144del+F157S+R158G+N211del+L212I+L216F+H245N+A264D+I332V+D339H+K356T+R403K+V445H+G446S+N450D+L452W+L455S+N460K+N481K+V483del+A484K+F486P+R493Q+E554K+A570V+P621S+H681R+S939F+P1143L). G*ΔG-VSV (VSV-G pseudotyped virus; Kerafast) and SARS-CoV-2 spike plasmid were transfected to 293T cells (CRL-3216; ATCC). After culture, the pseudovirus in the supernatant was collected, filtered, aliquoted and frozen at −80 °C for further use.

The Huh-7 cell line (0403; Japanese Collection of Research Bioresources) was used in pseudovirus neutralization assays. Purified mAbs were serially diluted in culture media, mixed with pseudovirus and incubated for 1 h in a 37 °C incubator with 5% CO_2. Then the digested Huh-7 cells were seeded in the antibody–virus mixture. After 1 day of culture in the incubator, the supernatant was discarded and D-luciferin reagent (DD1209-03; Vazyme) was added to the plates. After 2 min incubation in darkness, the cell lysate was transferred to detection plates. The luminescence values were detected and recorded with a microplate spectrophotometer (HH3400; PerkinElmer). IC_{50} was determined by fitting four-parameter logistic regression models.

Authentic virus propagation and titration

Authentic SARS-CoV-2 Omicron variant XBB.1.5.6 was kindly provided by the Rega Institute Leuven. Live Omicron variant BA.2.86 sublineage JN.3 was kindly provided by the Medicines and Healthcare Product Regulatory Agency.

Viral propagation of both strains was carried out as previously described[52]. Briefly, 175 cm^2 flasks were inoculated with Vero E6 cells diluted in complete DMEM 2% FBS (1×10^6 cells ml^{-1}). Cells were incubated at 37 °C, 5% CO_2 in a humidified atmosphere for 20–24 h, then the subconfluent cell monolayer was washed 2× with sterile Dulbecco's phosphate buffered saline (PBS) and inoculated with the SARS-CoV-2 virus at a multiplicity of infection of 0.001. After 1 h at 37 °C, 5% CO_2, the flasks were filled with 50 ml of complete DMEM 2% FBS and kept at 37 °C, 5% CO_2. Flasks were inspected daily under an optical microscope to check for signs of cytopathic effect (CPE) in the Vero E6 monolayer. Once CPE developed in at least 80–90% of the cell monolayer, the supernatants of the infected cell culture were collected, centrifuged at 1,000 rpm (106*g*) for 5 min (4 °C), aliquoted and stored at −80 °C.

For the viral escape assay, titration of the propagated Omicron variant XBB.1.5.6 was performed in 96-well plates containing confluent Vero E6 cells using the 50% tissue culture infectious dose ($TCID_{50}$) assay. Cells infected with serial 10-fold dilutions of the virus (from 10^{-1} to 10^{-11}) were incubated at 37 °C, 5% CO_2 and monitored for signs of virus-induced CPE under an inverted optical microscope for 4 days. The endpoint viral titre, defined as the reciprocal of the highest viral dilution resulting in at least 50% CPE in the inoculated wells, was calculated according to the Reed and Muench formula[53]. Titration of plaque forming unit (PFU) per millilitre of SARS-CoV-2 Omicron XBB.1.5.6 and JN.3 variants was performed in pre-seeded Vero E6 cells in 96-well plates. Briefly, cells were infected with serial 0.5-log-fold dilutions of the virus (from 10^{-1} to 10^{-6}) and incubated for 24 h at 37 °C, 5% CO_2. The viral titre was calculated by PFU counting.

Authentic virus escape mutant escape assay

For the authentic virus escape assay, an experimentally determined concentration of authentic XBB.1.5.6 virus was sequentially passaged in Vero E6 cells in the presence of serially diluted SARS-CoV-2-specific mAb (BD55-1205). The viral escape assay was performed as previously reported[52]. Briefly, 12 serial 2-fold dilutions of each antibody sample

were prepared in DMEM 2% FBS (with a 20 µg ml^{-1} starting concentration of antibody before virus addition). Each serially diluted sample was added to the wells of a 24-well plate, pre-seeded with Vero E6 cells (2×10^5 cells per well). Then a virus solution containing 10^5 $TCID_{50}$ of authentic SARS-CoV-2 Omicron variant XBB.1.5.6 was dispensed in each antibody-containing well and in wells dedicated to virus-only control.

The plates were then incubated for 1 h at 37 °C, 5% CO_2 to allow binding of the antibody sample to the virus. The virus–sample mixture was then transferred into the wells of a 24-well plate containing previously seeded Vero E6 cells to allow their infection from the unbound residual virus. The plates were incubated for 7 days at 37 °C, 5% CO_2 and cells were then examined for the presence of virus-induced CPE using an inverted optical microscope. The content of the well corresponding to the highest antibody concentration showing complete CPE was collected and further diluted to be used as the viral solution in the next virus passage. The potency of each antibody was recorded at each virus passage and expressed as inhibitory concentration 100% (that is, the lowest antibody concentration inhibiting development of CPE). The virus pressured with SARS-CoV-2 antibody was passaged in cell cultures along with the antibody sample of interest until CPE was observed at higher antibody concentrations. At each passage, both the virus pressured with the antibody sample of interest and the virus-only control were collected, propagated for 1 round of passaging in different 25 cm^2 flasks (pre-seeded with 1×10^5 Vero E6 cells ml^{-1}), aliquoted and stored at −80 °C to be used for RNA extraction and sequencing. The sequences of both these types of sample can assist in distinguishing between adaptation to cell culture conditions and escape mutations. Parallel titrations of each antibody-pressured virus were performed at every passage in 96-well plates containing pre-seeded Vero E6 cells (1.5×10^4 cells per well) to monitor the viral titre at each test.

RNA extraction

The RNA extraction to obtain the viral genetic material for next-generation sequencing was performed using the Biocomma Nucleic Acid Purification Kit (Spin Column; MNP027-1E; Biocomma), as described previously[52]. Briefly, 300 µl of viral sample was mixed with 500 µl Buffer GLX, vortexed for 1 min and incubated at room temperature (RT) for at least 5 min to allow virus lysis. The supernatant was then transferred into a spin column inserted in a collection tube and centrifuged at 12,000 rpm (15,287*g*) for 1 min at RT. After discarding the flow-through, 500 µl of Buffer PD (previously re-suspended with isopropanol) was added, centrifuged as before and the resulting flow-through was then discarded. The column was then washed with 700 µl of Buffer PW (previously re-suspended in absolute ethanol), centrifuged and eluted as before. This step was repeated twice. The spin column was then centrifuged at 12,000 rpm (15,287*g*) for 2 min and left with an open lid for 5 min to allow evaporation of residual ethanol. The column was placed in a new collection tube and 60 µl of RNAse-free ddH_20 were added. After a 2 min incubation at RT, the column was centrifuged for 2 min at 12,000 rpm (15,287*g*) to elute and collect the RNA, which was stored at −80 °C until shipment for sequencing.

Deep sequencing of authentic virus from escape assay and data analysis

The cDNA preparation was performed in a total volume of 40 µl by following the manufacturer's recommendations for SuperScript II Reverse Transcriptase (18064022; Life Technologies), Random Hexamers (50 µM; N8080127; Euroclone) and RNaseOUT Recombinant Ribonuclease Inhibitor (10777019; Life Technologies) using a thermocycler. SARS-CoV-2 genome amplicons were generated using the ARTIC v.3.5.2 panel (catalogue number 10016495; IDT), together with a set of custom oligo pools to improve coverage on the RBD domain sequence. The Celero DNA-Seq kit (NuGEN) was then used for library preparation, following the manufacturer's instructions. Both input and final libraries were quantified using the Qubit 2.0 Fluorometer (Invitrogen) and quality tested by the Agilent 2100 Bioanalyzer High Sensitivity DNA assay (Agilent Technologies). Libraries were then prepared for sequencing and sequenced on an Illumina NovaSeq6000 (Illumina) in paired-end 150 mode to generate a minimum of 5 million reads per sample.

Raw sequencing reads were first processed by removing PCR primer sequences using Cutadapt v.2.6, with parameters set to discard untrimmed pairs and ensure a minimum read length of 50 bp. Quality trimming was performed with Fastp v.0.20.0 to retain bases with a Phred score ≥Q30. The resulting high-quality reads were aligned to the NCBI Reference Sequence accession OQ063792.1. Subsequent filtering using a custom script removed reads with low mapping quality or suboptimal alignment characteristics. Variants were identified using GATK HaplotypeCaller v.4.1.6.0 and normalized with Bcftools norm v.1.9. A consensus sequence for each sample was generated by applying filtered variants to the reference sequence using Bcftools consensus, with low-coverage positions masked. Coverage was assessed using Bedtools genomecov v.2.29.2.

Authentic virus plaque reduction neutralization

Determination of IC_{50} was performed in Vero E6 cells by immunodetection of viral antigen. Briefly, 100 PFU per well of SARS-CoV-2 Omicron XBB.1.5.6 or Omicron JN.3 were incubated for 1 h with 5% CO_2 with serial 4-fold dilutions of mAbs (range 50–0.003 nM). At the end of the incubation, pre-seeded Vero E6 cells in 96-well plates were adsorbed with virus–sample mixture for 1 h at 37 °C with 5% CO_2. After removal of the virus inoculum, the overlay medium was added at each well and plates were incubated for 24 h at 37 °C with 5% CO_2.

The immunodetection assay was performed as described previously[54] with minor modifications. Briefly, cells were fixed for 3 h with 10% formalin (HT501320; Sigma-Aldrich) and permeabilized for 20 min with 0.1% Triton X-100 (1.08603; Sigma-Aldrich). After washing with PBS 1X (28348; Thermo Fisher) containing 0.05% Tween 20 (Sigma-Aldrich), plates were incubated for 1 h with SARS-CoV-2 nucleocapsid mouse mAb (A02048; GenScript) diluted 1:1,000 in blocking buffer (PBS 1X containing 1% BSA (A8327; Sigma-Aldrich) and 0.1% Tween 20). After washing, cells were incubated for 1 h with a polyclonal horseradish-peroxidase-coupled anti-mouse IgG secondary antibody (31430; Thermo Fisher) diluted 1:2,000 in blocking buffer. Next, cells were washed and the TrueBlue Peroxidase Substrate (5510-0030; Sera Care) was added to each well.

Detection of microplaques was performed using a ImmunoSpot S6 Ultra-V Analyzer (C.T.L.) reader using BioSpot software according to instrument specifications. The IC_{50} for each sample was calculated with GraphPad Prism software (v.9.0.1) using the dose–response inhibition category and applying the equation log(inhibitor) versus normalized response – variable slope.

Neutralization assays to SARS-CoV-2 WT (Wuhan-Hu-1), BA.1 (EPI_ISL_8187354), BA.5.2.1 (EPI_ISL_17261619.2) and FL.8 (XBB.1.9.1.8, EPI_ISL_17262369) authentic viruses were performed in a different laboratory. In brief, purified BD55-1205 is subsequently diluted in 2-fold serial dilutions from 500 ng ml^{-1} to 0.244 ng ml^{-1}. These diluted antibodies were mixed with live virus suspension containing 100 $TCID_{50}$ and added to 96-well plates at a 1:1 ratio. The plates were incubated in a 36.5 °C incubator with 5% CO_2 for 2 h. After incubation, Vero cells (a gift from the World Health Organization; CCL-81; ATCC) were added to each well containing the antibody–virus mixture. The plates were further incubated for 5 days in an incubator with 5% CO_2 at 36.5 °C. CPEs were evaluated by microscopy, and the IC_{50} values were determined by fitting two-parameter Hill equations. Experiments were conducted in four biological replicates in a biosafety level 3 facility.

Preparation of spike-pseudotyped rVSV

Similar to previous reports, SARS-CoV-2 XBB.1.5 S-pseudotyped rVSV was constructed and rescued from DNA clones[55,56]. In brief, the VSV G

gene on the plasmid encoding VSV antigenome with the T7 promoter was replaced by the codon-optimized SARS-CoV-2 XBB.1.5 spike gene with a carboxy-terminal 21-aa deletion. The GFP reporter gene was inserted into the VSV genome before the spike gene. BHK21 cells were infected with the vaccinia virus vTF7-3 that expresses T7 polymerase for 2 h, and the supernatant was discarded. The VSV antigenome plasmid and helper plasmids encoding VSV N, P, G and L genes (EH1013-1016; Kerafast) were co-transfected to the cells using Lipofectamine 3000. After 48 h incubation, the supernatant was collected, filtered by a 0.22 μm filter and passaged in Vero E6 cells. The virus was passaged every 2–3 days. After three to four rounds of amplification, the viral RNA was extracted and amplified by reverse transcription PCR. The spike gene was then amplified and sequenced for validation. The supernatant that contains the rescued virus was aliquoted and stored at −80°C.

rVSV-based escape mutation screening under antibody pressure

mAbs were prepared at concentrations of 5 μg ml^{-1}, 1.25 μg ml^{-1}, 0.3125 μg ml^{-1} and 0.078 μg ml^{-1} in DMEM (SH30243.01; Hyclone) supplemented with 2% FBS (SH30406.05; Hyclone). In some replicates, an additional concentration of 20 μg ml^{-1} was also included. A 0.5 ml volume of each dilution was added to individual wells of a 24-well plate. Subsequently, 0.5 ml of XBB.1.5 S-pseudotyped rVSV with a titre of 4×10^6 focus-forming units per millilitre was introduced to each well, resulting in a total volume of 1 ml per well. The plates were incubated at RT for 30 min to allow antibody–virus binding.

After incubation, 200 μl of Vero cell suspension (1×10^6 cells ml^{-1}) was added to each well, bringing the final volume to 1.2 ml. The cell–virus–antibody mixture was then cultured at 37 °C in an atmosphere containing 5% CO_2 for 72 h. The fluorescence signal, indicating successful viral entry and replication, was captured using a BioTek Cytation 5 Cell Imaging Multimode Reader (Agilent).

For the viral passage experiment, the supernatants from GFP-positive wells that contained the highest concentration of antibodies were collected. The samples were centrifuged at 350*g* for 3 min, the clarified supernatants were diluted in DMEM supplemented with 2% FBS, mixed with antibodies at various concentrations and then incubated for 30 min before the addition of Vero cells. Subsequent passages were performed under identical conditions to those of the initial experiment, until the virus could successfully infect cells (GFP$^+$) under antibody pressure at the highest concentration.

Recombinant RBD expression and purification

DNA fragments that encode SARS-CoV-2 variant RBD (spike 319-541) were codon optimized for human cell expression and synthesized by GenScript. His-AVI tags were added at the end of the RBD gene fragments. The fragments were then inserted into pCMV3 vectors through infusion (Vazyme). The recombination products were transformed into *Escherichia coli* DH5α competent cells (Tsingke). Colonies with the desired plasmids were confirmed by Sanger sequencing (Azenta) and cultured for plasmid extraction (CWBIO). Expi293F cells were transfected with the constructed plasmids and cultured for 6 days. The products were purified using Ni-NTA columns (SA005100; Changzhou Smart-Lifesciences) and the purified samples were verified by SDS–PAGE.

Surface plasmon resonance

Surface plasmon resonance experiments were performed on the Biacore 8K (Cytiva). mAbs (human IgG1) were immobilized onto Protein A sensor chips (29127556; Cytiva). Purified SARS-CoV-2 variant RBDs were prepared in serial dilutions (1.5625 nM, 3.125 nM, 6.25 nM, 12.5 nM, 25 nM and 50 nM) and injected over the sensor chips. The response units were recorded by the Biacore 8K Control Software (v.4.0.8.19879; Cytiva) at RT and the raw data curves were fitted to a 1:1 binding model to determine the affinities (dissociation constants) using Biacore 8K Evaluation Software (v.4.0.8.20368; Cytiva).

Protein expression and purification for cryo-EM

The spike gene of XBB.1.5 (containing the mutations T19I, Δ24–26, A27S, V83A, G142D, Δ144, H146Q, Q183E, V213E, G252V, G339H, R346T, L368I, S371F, S373P, S375F, T376A, D405N, R408S, K417N, N440K, V445P, G446S, N460K, S477N, T478K, E484A, F486P, F490S, R493Q, Q498R, N501Y, Y505H, D614G, H655Y, N679K, P681H, N764K, D796Y, Q954H and N969K) and the XBB.1.5 RBD were generated by overlapping PCR using the full-length S gene (residues 1–1,208; GenBank:MN908947) as template. The S gene was cloned into the vector pCAGGS with a T4 fibritin trimerization motif, an HRV3C protease site, and a Twin-Strep-tag at the carboxy-terminal of the spike and RBD sequences to facilitate protein purification, and was then mutated as previously described[57]. All the constructed vectors were transiently transfected into suspended FreeStyle 293-F cells (R79007; Thermo Fisher) and cultured at 37 °C in a rotating, humidified incubator supplied with 8% CO_2 and maintained at 130 rpm (0.25*g*). After incubation for 72 h, the supernatant was collected, concentrated and exchanged into the binding buffer using a tangential flow filtration cassette. The S proteins were then separated by chromatography using resin attached with streptavidin and further purified by size exclusion chromatography using a Superose 6 10/300 (GE Healthcare) in 20 mM Tris, 200 mM NaCl, pH 8.0.

Production of Fab fragment

To generate the Fab fragments for cryo-EM analyses, the purified antibodies were processed using the Pierce Fab Preparation Kit (44895; Thermo Fisher) as described previously[13]. Briefly, the samples were first applied to desalination columns to remove the salt. After centrifugation, the flow-through was collected and incubated with beads attached with papain to cleave Fab fragments from the whole antibodies. The mixtures were then transferred to a Protein A affinity column, which specifically binds the Fc fragments of antibodies. After centrifugation, the Fab fragments were obtained and dialysed into PBS.

Cryo-EM sample collection, data acquisition and structure determination

The cryo-EM samples of S trimers were prepared in complex with BD55-1205 at a molar ratio of 1:4 (S protein:BD55-1205) on ice to obtain the S–BD55-1205 complex. Then the complex was deposited onto the freshly glow-discharged grids (C-flat 1.2 by 1.3 Au). After 6 s of blotting in 100% relative humidity, the grid was plunged into liquid ethane automatically by Vitrobot (FEI). Cryo-EM datasets were collected using a 200 kV FEI Talos Arctica microscope equipped with a K2 detector. Videos (32 frames, each 0.2 s, total dose of 60 e Å^{-2}) were recorded with a defocus range between 1.5 μm and 2.7 μm. Automated single particle data acquisition was carried out by SerialEM, with a calibrated magnification of 75,000, yielding a final pixel size of 1.04 Å. A total of 5,722 micrographs were collected. CryoSPARC (v.4.4.1) was used to correct beam-induced motion and average frames. The defocus value of each micrograph was then estimated using the patch contrast transfer function (CTF) estimation. A total of 2,515,383 particles of the XBB.1.5 S–BD55-1205 complex were autopicked and extracted for further two-dimensional (2D) classification and heterogeneous refinement. After that, 238,788 particles of the XBB.1.5 S–BD55-1205 complex were used for homogeneous refinement in cryoSPARC for the final cryo-EM density.

To improve the resolution of the RBD–antibody binding surface, the cryo-EM sample of XBB.1.5 RBD in complex with BD55-1205 and BD57-0120 Fab, which is another RBD-targeting mAb that does not compete with BD55-1205, was also deposited. This approach allowed us to deduce a more accurate epitope and paratope than was achievable using the flexible-up RBD conformation in the BD55-1205–S cryo-EM structure, with BD57-0120 Fab used to increase the molecular weight of the complex. We performed asymmetric reconstruction of the complex structure, achieving an overall resolution of 3.3 Å, enabling reliable analysis of the interaction interface. The cryo-EM samples of XBB.1.5

RBD in complex with BD55-1205 were mixed in a molar ratio of 1:1.2:1.2 (RDB:BD55-1205:BD57-0120). Videos (32 frames, each 0.2 s, total dose of 60 e Å^{-2}) were recorded using a Falcon 4 Summit direct detector with a defocus range between 1.2 µm and 1.8 µm. Automated single-particle data acquisition was carried out by EPU, with a calibrated magnification of 96,000, yielding a final pixel size of 0.808 Å. A total of 5,866 micrographs for the XBB.1.5 RBD–BD55-1205/BD57-0120 complex were collected. CryoSPARC was used to correct beam-induced motion and average frames. The defocus value of each micrograph was then estimated by patch CTF estimation. A total of 3,186,044 particles of the XBB.1.5 RBD–BD55-1205/BD57-0120 complex were autopicked and extracted for further 2D classification and heterogeneous refinement. After that, 266,321 particles of the XBB.1.5 RBD–BD55-1205/BD57-0120 complex were used for homogeneous refinement and non-uniform refinement in cryoSPARC for the final cryo-EM density.

The resolutions were evaluated on the basis of the gold-standard Fourier shell correction (threshold of 0.143) and evaluated using ResMap (v.1.1.4). All dataset processing is shown in Extended Data Fig. 6.

Structure model fitting and refinement

The atomic models of the complex were first generated by fitting the chain of the apo (PDB:7XNQ) and Fab (predicted by AlphaFold) into the obtained cryo-EM density using Chimera (v.1.5). The structure was then manually adjusted and corrected according to the protein sequences and density in Coot (v.0.9.8.91), and real-space refinement was performed using Phenix (v.1.20.1).

Generation of modified mRNA and LNPs

BD55-1205 with the 'LA' modification and CHKV-24 with the 'LS' modification (for consistency with historical data) were used in the studies. Sequence-optimized mRNAs encoding functional IgG mAbs were synthesized in vitro using an optimized T7 RNA polymerase-mediated transcription reaction, with complete replacement of uridine by N1-methyl-pseudouridine[58]. The reactions included a DNA template containing an open reading frame flanked by 5′ and 3′ untranslated region (UTR) sequences, with a terminally encoded poly(A) tail. Free mRNA was purified, buffer exchanged and sterile filtered.

LNP-formulated mRNA was produced through a modified ethanol-drop nanoprecipitation process as described previously[47,50,59–62]. Briefly, ionizable, structural, helper and polyethylene glycol lipids were mixed with mRNA in acetate buffer at a pH of 5.0 and at a ratio of 3:1 (lipids:mRNA), with a 2:1 ratio of HC to LC. The mixture was neutralized with Tris-Cl at a pH of 7.5, sucrose was added as a cryoprotectant and the final solution was sterile filtered. Vials were filled with formulated LNP and stored frozen at −70 °C until further use. All formulations underwent analytical characterization for particle size, RNA encapsulation, mRNA purity, osmolarity and endotoxin levels. They were found to be between 80 nm and 100 nm in size, with greater than 90% encapsulation, <1 EU ml^{-1} of endotoxin and were deemed acceptable for in vivo study.

Moderna's proprietary UTR sequences for enhancing mRNA stability and translation efficiency are protected under US patent number 11389546, and the methods for LNP composition and delivery are protected under US patent number 11285222.

Expression of mAbs in mice

Homozygous Tg32-SCID mice (B6.Cg-*Fcgrt*^{tm1Dcr} *Prkdc*^{scid} Tg(FCGRT)32Dcr/DcrJ; catalogue number 018441) and Tg32 mice (B6.Cg-*Fcgrt*^{tm1Dcr} Tg(FCGRT)32Dcr/DrJ; catalogue number 014565) were obtained from The Jackson Laboratory. Animals were housed in groups of 4, fed standard chow diets, subjected to a photoperiod of 12 h light/12 h dark cycle and kept at an ambient animal RT of 70° ± 2° F with a room humidity of 50% ± 5%.

Six- to eight-week-old female Tg32-SCID mice (2 groups, 4 mice in each group) or male (1 group with 4 mice) and female (1 group with 4 mice) Tg32 mice (The Jackson Laboratory) were injected intravenously with the indicated mRNA-LNP at the indicated dose (0.5 mg kg^{-1}) in 100 µl total volume. All mRNA-LNPs for in vivo studies were prepared by co-formulations of HC and LC for the expression of the full IgG. Mice were bled via submandibular vein at the indicated time points and serum was isolated for antibody quantification by ELISA and assessment of serum neutralizing titre. At the final indicated time point, mice were killed via CO_2 asphyxiation and a terminal bleed was collected via cardiac puncture.

Mouse serum ELISA for human IgG quantification

To quantitate total human IgG (hIgG), 96-well NUNC Maxisorp plates (439454; Thermo Scientific) were coated with 0.1 ml per well of goat anti-human IgG Fc fragment (A80-104A; Bethyl) at a 1:100 dilution in 0.05 M carbonate-bicarbonate (C30411; Sigma) overnight at 4 °C. Plates were washed with an automated plate washer (Biotek) 4× with 0.05% PBST and were subsequently blocked with 0.2 ml SuperBlock PBST (37515; Thermo Fisher) per well for 1.5 h at 37 °C. Using purified antibodies as a standard, mRNA transfection supernatant or mouse serum was serially diluted in PBST in a dilution plate and 0.1 ml per well was transferred to the coated plates and incubated for 2 h at 37 °C. Following incubation, plates were subsequently washed and incubated with 0.1 ml per well of goat anti-human IgG horseradish peroxidase (1:5,000; 2040-05; Southern Biotech) for 1 h at 37 °C. Plates were subsequently washed and incubated with 0.1 ml per well of SureBlue TMB 1-C substrate (52-00-04; SeraCare) for 10 min. The reaction was stopped with 0.1 ml per well of TMB Stop solution (50-85-05; SeraCare) and read at an absorbance of 450 nm on a SpectraMax ABS Microplate Reader (Molecular Devices). Absolute quantities of human antibody in transfection supernatant or mouse serum were extrapolated using GraphPad Prism (v.9.0.1) using a standard curve.

Mouse serum pseudovirus neutralization assays

Codon-optimized full-length spike genes (XBB.1.5, JN.1 and HK.3.1) were cloned into a pCAGGS vector. Spike genes contained the following mutations: (1) for XBB.1.5, T19I, L24–P26del, A27S, V83A, G142D, Y144del, H146Q, Q183E, V213E, G252V, G339H, R346T, L368I, S371F, S373P, S375F, T376A, D405N, R408S, K417N, N440K, V445P, G446S, N460K, S477N, T478K, E484A, F486P, F490S, Q498R, N501Y, Y505H, D614G, H655Y, N679K, P681H, N764K, D796Y, Q954H and N969K; (2) for JN.1, V16–17insMPLF, T19I, R21T, L24–P26del, A27S, S50L, H69–V70del, V127F, G142D, Y144del, F157S, R158G, N211del, L212I, V213G, L216F, H245N, A264D, I332V, G339H, K356T, S371F, S373P, S375F, T376A, R403K, D405N, R408S, K417N, N440K, V445H, G446S, N450D, L452W, L455S, N460K, S477N, T478K, N481K, V483del, E484K, F486P, Q498R, N501Y, Y505H, E554K, A570V, D614G, P621S, H655Y, N679K, P681R, N764K, D796Y, S939F, Q954H, N969K and P1143L; and (3) for HK.3.1, T19I, L24–P26del, A27S, Q52H, V83A, G142D, Y144del, H146Q, F157L, Q183E, V213E, G252V, G339H, R346T, L368I, S371F, S373P, S375F, T376A, D405N, R408S, K417N, N440K, V445P, G446S, L455F, F456L, N460K, S477N, T478K, E484A, F486P, F490S, Q498R, N501Y, Y505H, D614G, H655Y, N679K, P681H, N764K, D796Y, Q954H and N969K. To generate VSVΔG-based SARS-CoV-2 pseudovirus, BHK-21/WI-2 cells were transfected with the spike expression plasmid and infected by VSVΔG-firefly-luciferase as previously described[63]. Vero E6 cells were used as target cells for the neutralization assay and maintained in DMEM supplemented with 10% FBS. To perform the neutralization assay, mouse serum samples were heat inactivated for 45 min at 56 °C and serial dilutions were made in DMEM supplemented with 10% FBS. The diluted serum samples or culture medium (serving as virus-only control) were mixed with VSVΔG-based SARS-CoV-2 pseudovirus and incubated at 37 °C for 45 min. The inoculum virus or virus–serum mix was subsequently used to infect Vero E6 cells (CRL-1586; ATCC) for 18 h at 37 °C. At 18 h after infection, an equal volume of One-Glo reagent (E6120; Promega) was

added to the culture medium for read-out using a BMG PHERastar-FSX plate reader. The percentage of neutralization was calculated based on relative light units of the virus control and subsequently analysed using a four-parameter logistic curve (GraphPad Prism 8.0).

Statistics and reproducibility

The sample sizes in this study (number of experimental measurement replicates and number of animals) were based on experience and were sufficient for the necessary statistical tests. Experimental assays were performed in at least two independent experiments. No statistical method was used to predetermine sample size. A total of 668 mAbs were excluded from the study because of insufficient amount of antibody and missing neutralization data to D614G or autologous pseudovirus. No data were excluded from the analyses. Results of all replicates are shown in the figures. The experiments were not randomized. The investigators were not blinded to allocation during experiments and outcome assessments.

In Fig. 2e, enrichment of Omicron-effective NAbs among NAbs neutralizing designed mutants is indicated by hypergeometric tests, based on the number of mAbs with an IC_{50} to a designed mutant of <0.05 μg ml^{-1} and the number of mAbs with an IC_{50} to a real-world Omicron strain of <0.05 μg ml^{-1}. In Fig. 5c,e, we used Wilcoxon rank-sum tests to determine whether there are significant differences between mice groups. Non-parametric Wilcoxon tests do not assume the data normality. For *t*-tests involved in the calculation of Pearson's correlation, data distribution was assumed to be normal but this was not formally tested. Illustration was performed using PyMOL (v.2.6.0a0), the Python package logomaker (v.0.8), the R package ggplot2 (v.3.4.4) and ComplexHeatmap (v.2.14).

Reporting summary

Further information on research design is available in the Nature Portfolio Reporting Summary linked to this article.

Data availability

Information about the mAbs involved in this study is included in Supplementary Table 1. Cryo-EM data for structures have been deposited in the Protein Data Bank (PDB), with accession codes 8XE9 and 8XEA, and in the Electron Microscopy Data Bank (EMDB), with accession codes EMD-38283 and EMD-38284. Other necessary source data to reproduce the analyses and illustrations have been deposited in Zenodo (https://doi.org/10.5281/zenodo.15294998)[64]. Additional materials and data are available from the lead corresponding author (Y.C.) upon request and are subject to a Material and Data Transfer Agreement. All enquiries will be replied to within 7 working days. Source data are provided with this paper.

Code availability

The custom scripts for data analysis and illustrations involved in this study have been deposited on GitHub (https://github.com/yunlongcaolab/predict-identify-bnabs).

References

1. Sachs, J. D. et al. The Lancet Commission on lessons for the future from the COVID-19 pandemic. *Lancet* **400**, 1224–1280 (2022).
2. Carabelli, A. M. et al. SARS-CoV-2 variant biology: immune escape, transmission and fitness. *Nat. Rev. Microbiol.* **21**, 162–177 (2023).
3. Kaku, Y. et al. Antiviral efficacy of the SARS-CoV-2 XBB breakthrough infection sera against Omicron subvariants including EG.5. *Lancet Infect. Dis.* **23**, e395–e396 (2023).
4. Jian, F. et al. Convergent evolution of SARS-CoV-2 XBB lineages on receptor-binding domain 455–456 synergistically enhances antibody evasion and ACE2 binding. *PLoS Pathog.* **19**, e1011868 (2023).
5. Kaku, Y. et al. Virological characteristics of the SARS-CoV-2 JN.1 variant. *Lancet Infect. Dis.* https://doi.org/10.1016/S1473-3099(23)00813-7 (2024).
6. Yang, S. et al. Fast evolution of SARS-CoV-2 BA.2.86 to JN.1 under heavy immune pressure. *Lancet Infect. Dis.* https://doi.org/10.1016/S1473-3099(23)00744-2 (2023).
7. Wang, Q. et al. XBB.1.5 monovalent mRNA vaccine booster elicits robust neutralizing antibodies against XBB subvariants and JN.1. *Cell Host Microbe* **32**, 315–321.e3 (2024).
8. Dougan, M. et al. Bamlanivimab plus etesevimab in mild or moderate COVID-19. *N. Engl. J. Med.* **385**, 1382–1392 (2021).
9. Gupta, A. et al. Early treatment for COVID-19 with SARS-CoV-2 neutralizing antibody sotrovimab. *N. Engl. J. Med.* **385**, 1941–1950 (2021).
10. Weinreich, D. M. et al. REGN-COV2, a neutralizing antibody cocktail, in outpatients with COVID-19. *N. Engl. J. Med.* **384**, 238–251 (2020).
11. Kelley, B. Developing therapeutic monoclonal antibodies at pandemic pace. *Nat. Biotechnol.* **38**, 540–545 (2020).
12. Bruel, T. et al. Serum neutralization of SARS-CoV-2 Omicron sublineages BA.1 and BA.2 in patients receiving monoclonal antibodies. *Nat. Med.* **28**, 1297–1302 (2022).
13. Cao, Y. et al. Omicron escapes the majority of existing SARS-CoV-2 neutralizing antibodies. *Nature* **602**, 657–663 (2022).
14. Cao, Y. et al. BA.2.12.1, BA.4 and BA.5 escape antibodies elicited by Omicron infection. *Nature* **608**, 593–602 (2022).
15. Iketani, S. et al. Antibody evasion properties of SARS-CoV-2 Omicron sublineages. *Nature* **604**, 553–556 (2022).
16. Cox, M. et al. SARS-CoV-2 variant evasion of monoclonal antibodies based on in vitro studies. *Nat. Rev. Microbiol.* **21**, 112–124 (2023).
17. Cameroni, E. et al. Broadly neutralizing antibodies overcome SARS-CoV-2 Omicron antigenic shift. *Nature* **602**, 664–670 (2022).
18. Park, Y. J. et al. Antibody-mediated broad sarbecovirus neutralization through ACE2 molecular mimicry. *Science* **375**, 449–454 (2022).
19. Luo, S. et al. An antibody from single human VH-rearranging mouse neutralizes all SARS-CoV-2 variants through BA.5 by inhibiting membrane fusion. *Sci. Immunol.* **7**, eadd5446 (2022).
20. Nutalai, R. et al. Potent cross-reactive antibodies following Omicron breakthrough in vaccinees. *Cell* **185**, 2116–2131.e2118 (2022).
21. Hong, Q. et al. Molecular basis of receptor binding and antibody neutralization of Omicron. *Nature* **604**, 546–552 (2022).
22. Westendorf, K. et al. LY-CoV1404 (bebtelovimab) potently neutralizes SARS-CoV-2 variants. *Cell Rep.* **39**, 110812 (2022).
23. Bianchini, F. et al. Human neutralizing antibodies to cold linear epitopes and subdomain 1 of the SARS-CoV-2 spike glycoprotein. *Sci. Immunol.* **8**, eade0958 (2023).
24. Liu, L. et al. Antibodies targeting a quaternary site on SARS-CoV-2 spike glycoprotein prevent viral receptor engagement by conformational locking. *Immunity* **56**, 2442–2455.e2448 (2023).
25. Cao, Y. et al. Imprinted SARS-CoV-2 humoral immunity induces convergent Omicron RBD evolution. *Nature* **614**, 521–529 (2023).
26. Li, G., Hilgenfeld, R., Whitley, R. & De Clercq, E. Therapeutic strategies for COVID-19: progress and lessons learned. *Nat. Rev. Drug Discov.* **22**, 449–475 (2023).
27. Yisimayi, A. et al. Repeated Omicron exposures override ancestral SARS-CoV-2 immune imprinting. *Nature* **625**, 148–156 (2024).
28. Cao, Y. et al. Rational identification of potent and broad sarbecovirus-neutralizing antibody cocktails from SARS convalescents. *Cell Rep.* **41**, 111845 (2022).
29. Cao, Y. et al. Potent neutralizing antibodies against SARS-CoV-2 identified by high-throughput single-cell sequencing of convalescent patients' B cells. *Cell* **182**, 73–84.e16 (2020).

30. Cao, Y. et al. Humoral immune response to circulating SARS-CoV-2 variants elicited by inactivated and RBD-subunit vaccines. *Cell Res.* **31**, 732–741 (2021).
31. Starr, T. N. et al. Deep mutational scanning of SARS-CoV-2 receptor binding domain reveals constraints on folding and ACE2 binding. *Cell* **182**, 1295–1310.e1220 (2020).
32. Ju, B. et al. Infection with wild-type SARS-CoV-2 elicits broadly neutralizing and protective antibodies against Omicron subvariants. *Nat. Immunol.* **24**, 690–699 (2023).
33. Chen, Y. et al. Broadly neutralizing antibodies to SARS-CoV-2 and other human coronaviruses. *Nat. Rev. Immunol.* **23**, 189–199 (2023).
34. Li, H. et al. Establishment of replication-competent vesicular stomatitis virus-based recombinant viruses suitable for SARS-CoV-2 entry and neutralization assays. *Emerg. Microbes Infect.* **9**, 2269–2277 (2020).
35. Schmidt, F. et al. High genetic barrier to SARS-CoV-2 polyclonal neutralizing antibody escape. *Nature* **600**, 512–516 (2021).
36. Jian, F. et al. Evolving antibody response to SARS-CoV-2 antigenic shift from XBB to JN.1. *Nature* **637**, 921–929 (2024).
37. Taylor, A. L. & Starr, T. N. Deep mutational scanning of SARS-CoV-2 Omicron BA.2.86 and epistatic emergence of the KP.3 variant. *Virus Evol.* **10**, veae067 (2024).
38. Barnes, C. O. et al. SARS-CoV-2 neutralizing antibody structures inform therapeutic strategies. *Nature* **588**, 682–687 (2020).
39. Yuan, M. et al. Structural basis of a shared antibody response to SARS-CoV-2. *Science* **369**, 1119–1123 (2020).
40. Zemlin, M. et al. Expressed murine and human CDR-H3 intervals of equal length exhibit distinct repertoires that differ in their amino acid composition and predicted range of structures. *J. Mol. Biol.* **334**, 733–749 (2003).
41. Tuekprakhon, A. et al. Antibody escape of SARS-CoV-2 Omicron BA.4 and BA.5 from vaccine and BA.1 serum. *Cell* **185**, 2422–2433.e2413 (2022).
42. Du, S. et al. Structurally resolved SARS-CoV-2 antibody shows high efficacy in severely infected hamsters and provides a potent cocktail pairing strategy. *Cell* **183**, 1013–1023.e1013 (2020).
43. Levin, M. J. et al. Intramuscular AZD7442 (tixagevimab–cilgavimab) for prevention of COVID-19. *N. Engl. J. Med.* **386**, 2188–2200 (2022).
44. Schmidt, P. et al. Antibody-mediated protection against symptomatic COVID-19 can be achieved at low serum neutralizing titers. *Sci. Transl. Med.* **15**, eadg2783 (2023).
45. Roopenian, D. C., Christianson, G. J. & Sproule, T. J. in *Mouse Models for Drug Discovery: Methods and Protocols* (eds Proetzel, G. & Wiles, M. V.) 93–104 (Humana Press, 2010).
46. August, A. et al. A phase 1 trial of lipid-encapsulated mRNA encoding a monoclonal antibody with neutralizing activity against chikungunya virus. *Nat. Med.* **27**, 2224–2233 (2021).
47. Kose, N. et al. A lipid-encapsulated mRNA encoding a potently neutralizing human monoclonal antibody protects against chikungunya infection. *Sci. Immunol.* **4**, eaaw6647 (2019).
48. O'Brien, M. P. et al. Subcutaneous REGEN-COV antibody combination to prevent COVID-19. *N. Engl. J. Med.* **385**, 1184–1195 (2021).
49. Ison, M. G. et al. Prevention of COVID-19 following a single intramuscular administration of adintrevimab: results from a phase 2/3 randomized, double-blind, placebo-controlled trial (EVADE). *Open Forum Infect. Dis.* **10**, ofad314 (2023).
50. Deal, C. E. et al. An mRNA-based platform for the delivery of pathogen-specific IgA into mucosal secretions. *Cell Rep. Med.* **4**, 101253 (2023).
51. Nie, J. et al. Establishment and validation of a pseudovirus neutralization assay for SARS-CoV-2. *Emerg. Microbes Infect.* **9**, 680–686 (2020).
52. Andreano, E. et al. SARS-CoV-2 escape from a highly neutralizing COVID-19 convalescent plasma. *Proc. Natl Acad. Sci. USA* **118**, e2103154118 (2021).
53. Reed, L. J. & Muench, H. A simple method of estimating fifty per cent endpoints. *Am. J. Epidemiol.* **27**, 493–497 (1938).
54. Brai, A. et al. Exploring the implication of DDX3X in DENV infection: discovery of the first-in-class DDX3X fluorescent inhibitor. *ACS Med. Chem. Lett.* **11**, 956–962 (2020).
55. Wu, X. et al. Development of a bioluminescent imaging mouse model for SARS-CoV-2 infection based on a pseudovirus system. *Vaccines* **11**, 1133 (2023).
56. Lawson, N. D., Stillman, E. A., Whitt, M. A. & Rose, J. K. Recombinant vesicular stomatitis viruses from DNA. *Proc. Natl Acad. Sci. USA* **92**, 4477–4481 (1995).
57. Cui, Z. et al. Structural and functional characterizations of infectivity and immune evasion of SARS-CoV-2 Omicron. *Cell* **185**, 860–871.e813 (2022).
58. Nelson, J. et al. Impact of mRNA chemistry and manufacturing process on innate immune activation. *Sci. Adv.* **6**, eaaz6893 (2020).
59. Sabnis, S. et al. A novel amino lipid series for mRNA delivery: improved endosomal escape and sustained pharmacology and safety in non-human primates. *Mol. Ther.* **26**, 1509–1519 (2018).
60. Narayanan, E. et al. Rational design and in vivo characterization of mRNA-encoded broadly neutralizing antibody combinations against HIV-1. *Antibodies* **11**, 67 (2022).
61. Richner, J. M. et al. Vaccine mediated protection against Zika virus-induced congenital disease. *Cell* **170**, 273–283.e212 (2017).
62. Richner, J. M. et al. Modified mRNA vaccines protect against Zika virus infection. *Cell* **168**, 1114–1125.e10 (2017).
63. Whitt, M. A. Generation of VSV pseudotypes using recombinant ΔG-VSV for studies on virus entry, identification of entry inhibitors, and immune responses to vaccines. *J. Virol. Methods* **169**, 365–374 (2010).
64. Jian, F., & Cao, Y. Resources for "Viral evolution prediction identifies broadly neutralizing antibodies to existing and prospective SARS-CoV-2 variants". *Zenodo* https://doi.org/10.5281/zenodo.15294998 (2025).

Acknowledgements

This project is financially supported by the Ministry of Science and Technology of China (2022ZD0115002, Y.C.) and the National Natural Science Foundation of China (32222030, Y.C.). We acknowledge G. Piccini, A. Manenti and E. Montomoli and their laboratory team at VisMederi Srl, Sienna, Italy, and Z. Lv at Sinovac Inc. for their contributions to the methods and for performing authentic virus assays. We also thank the Medicines and Healthcare Product Regulatory Agency and P. Maes (Rega Institute Leuven) for providing the authentic SARS-CoV-2 viruses. We thank the team at IGA Technology Services and D. Scaglione for their contribution of authentic virus amplicon sequencing and data analysis services. We also thank K. Hardcastle and the Comparative Medicine team at Moderna for the planning and execution of the in vivo studies.

Author contributions

Y.C. designed and supervised the study. F.J., A.Z.W., L.M.W. and Y.C. wrote the manuscript with input from all authors. L.F., L.W. and X.W. solved and analysed the cryo-EM structures. Y.Y. and Youchun Wang constructed pseudoviruses. P.W. and F.J. performed the rVSV escape screening experiments and data analysis. J.H. performed the authentic virus escape assays and data analysis. L.Y. performed the surface plasmon resonance experiments. P.W., L.Y., T.X., Yao Wang and F.S. performed the pseudovirus neutralization assays. A.Y., W.S., X.N., R.A. and Yao Wang isolated the mAbs. J.W. (Changping Laboratory), L.L, L.Y.

and F.S. performed protein expression and purification experiments. J.W. (BIOPIC) and F.J. analysed the DMS data. S.Y., L.F. and F.J. performed sequence analysis and illustration. A.Z.W., S.P. and L.M.W. conceptualized and planned the mRNA delivery study. D.M.B., D.L. and T.S. performed the mouse serum neutralization assays and data analysis. L.M. and T.K. performed and supervised the pharmacokinetic ELISA assays.

Competing interests

Y.C. is listed as an inventor for provisional patent applications of SARS-CoV-2 RBD-specific antibodies involved in this study, including BD55-1205. The patent of BD55-1205 is licensed to Moderna. Y.C. is a co-founder of Singlomics Biopharmaceuticals. A.Z.W., J.H., D.M.B., D.L., T.S., L.M., T.K., S.P. and L.M.W. are full-time employees and holders of equity in Moderna Therapeutics. The other authors declare no competing interests.

Additional information

Extended data is available for this paper at https://doi.org/10.1038/s41564-025-02030-7.

Supplementary information The online version contains supplementary material available at https://doi.org/10.1038/s41564-025-02030-7.

Correspondence and requests for materials should be addressed to Xiangxi Wang, Laura M. Walker or Yunlong Cao.

Peer review information *Nature Microbiology* thanks Kizzmekia Corbett, Shaowei Li, Lizhou Zhang and the other, anonymous, reviewer(s) for their contribution to the peer review of this work.

[1]Biomedical Pioneering Innovation Center (BIOPIC), Peking University, Beijing, China. [2]Changping Laboratory, Beijing, China. [3]College of Chemistry and Molecular Engineering, Peking University, Beijing, China. [4]Moderna Inc., Cambridge, MA, USA. [5]CAS Key Laboratory of Infection and Immunity, National Laboratory of Macromolecules, Institute of Biophysics, Chinese Academy of Sciences, Beijing, China. [6]University of Chinese Academy of Sciences, Beijing, China. [7]School of Life Sciences, Peking University, Beijing, China. [8]Peking-Tsinghua Center for Life Sciences, Tsinghua University, Beijing, China. [9]Joint Graduate Program of Peking-Tsinghua-NIBS, Academy for Advanced Interdisciplinary Studies, Peking University, Beijing, China. [10]Institute of Medical Biology, Chinese Academy of Medical Science and Peking Union Medical College, Kunming, China. [11]These authors contributed equally: Fanchong Jian, Anna Z. Wec, Leilei Feng. ✉e-mail: xiangxi@ibp.ac.cn; laura.walker@modernatx.com; yunlongcao@pku.edu.cn

https://doi.org/10.1038/s41564-025-02030-7

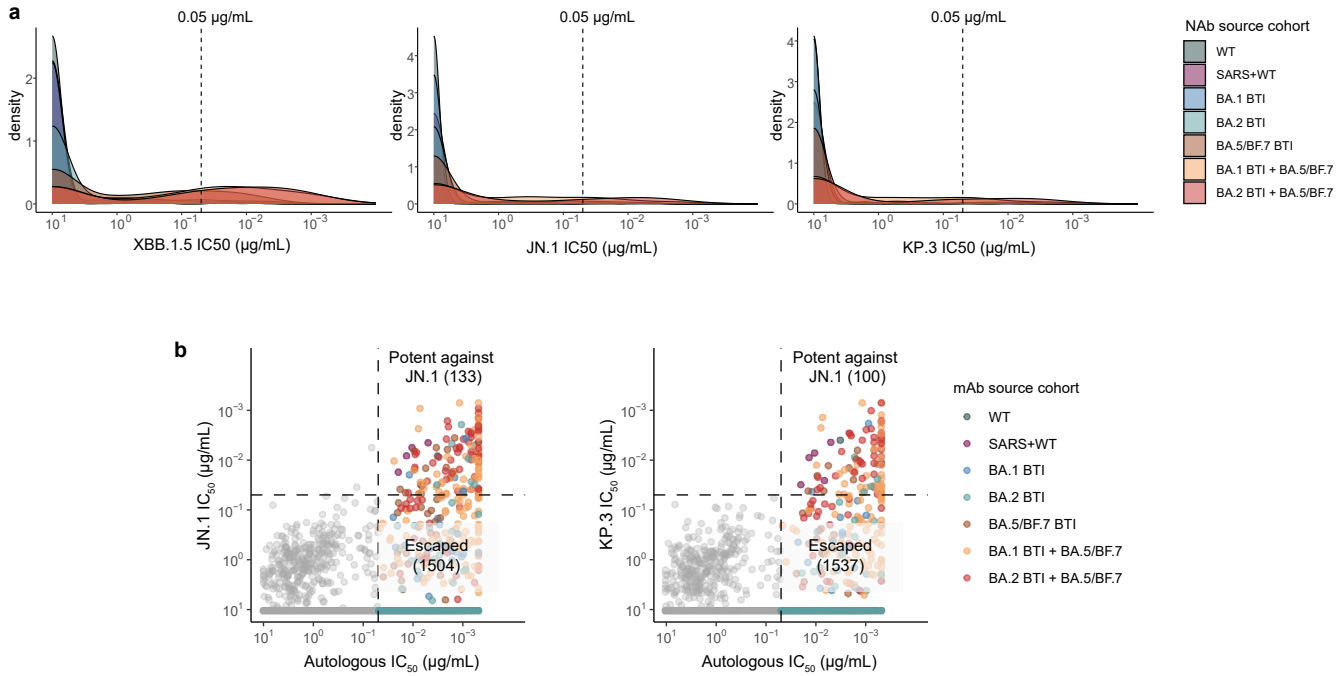

Extended Data Fig. 1 | Neutralization distribution of mAbs collected. a, Distribution of the neutralization activities (IC_{50}) of potent autologous NAbs against XBB.1.5 and JN.1. **b**, Scatter plots showing the relationship between the autologous neutralization activities and JN.1/KP.3-neutralizing activities of the isolated mAbs.

https://doi.org/10.1038/s41564-025-02030-7

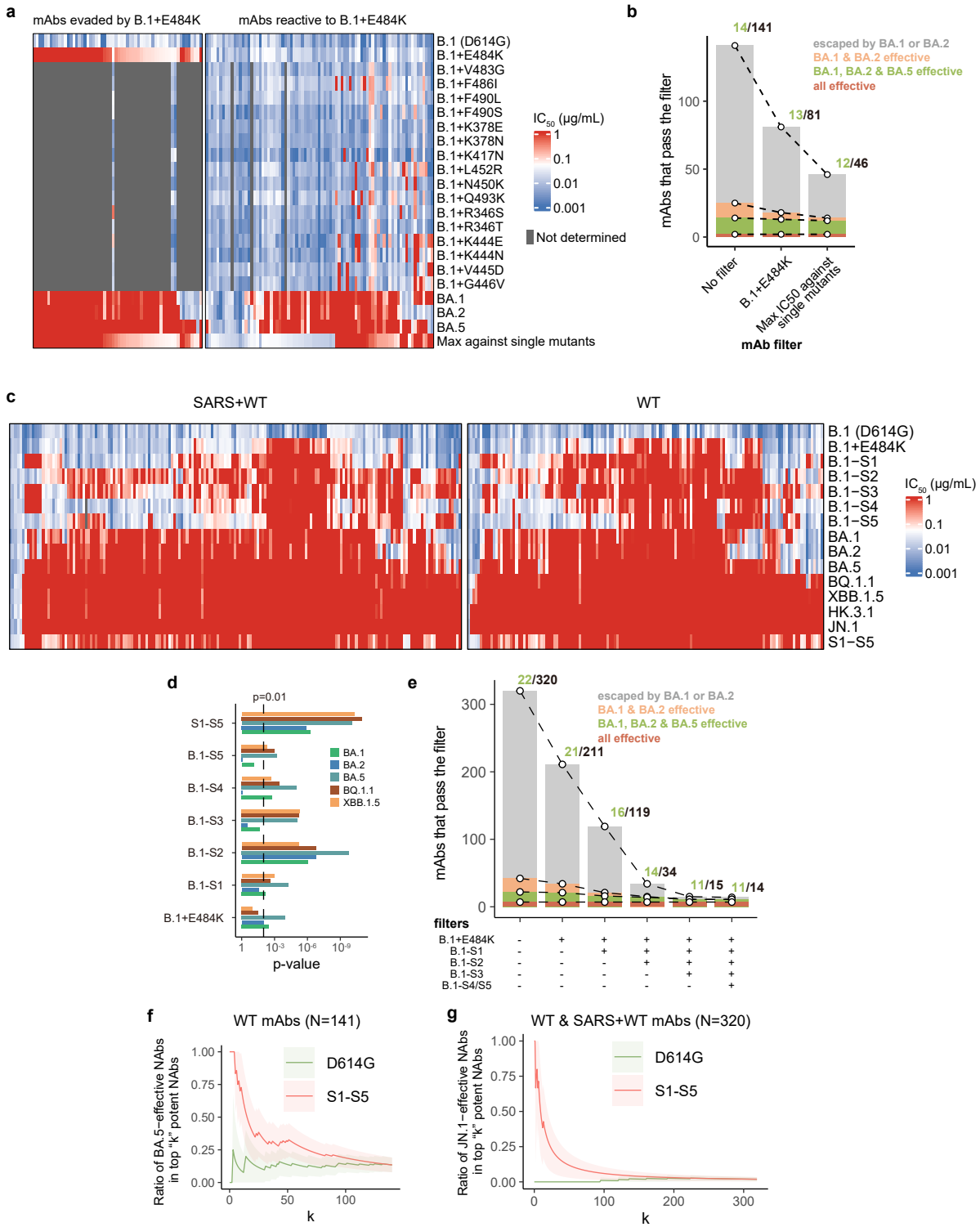

Extended Data Fig. 2 | Neutralization activities for the identification of bnAbs. **a**, Heatmap of the neutralization activities (IC_{50}) for the mAbs from SARS-CoV-2 WT cohort against the designed single mutants and Omicron variants. **b**, Number of NAbs from WT cohort that pass the filter of designed single mutants. Ratio of BA.1, BA.2, and BA.5-potent NAbs among the passed NAbs are annotated above the bar of each combination of filter. **c**, Heatmap of the neutralization activities (IC_{50}) for the mAbs from early cohorts (SARS+WT and WT) against the designed mutants and real-world Omicron variants. 'S1-S5' indicates the highest IC_{50} against the five designed mutants. **d**, Significance for the enrichment of BA.1, BA.2, BA.5, BQ.1.1, or XBB.1.5-potent NAbs within NAbs that were from WT or SARS+WT cohort pass each filter of designed mutants (two-sided hypergeometric test). **e**, Number of NAbs from WT or SARS+WT cohort that pass the filter of designed mutants. Ratio of BA.1, BA.2, and BA.5-potent NAbs among the passed NAbs are annotated. **f-g**, Ratio of BA.5 or JN.1-potent NAbs within the NAbs from WT cohort (**f**), or WT in addition to SARS+WT cohort (**g**) with 'top k' neutralization activities against D614G or S1-S5. The error bars indicate 95% confidence interval under normal distribution.

https://doi.org/10.1038/s41564-025-02030-7

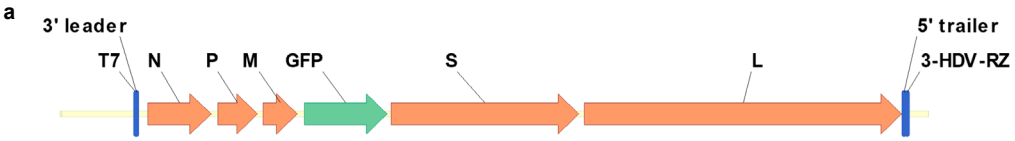

b

Pseudovirus IC_{50} (ng/mL)

antibody	source	SARS-CoV-1	D614G	BA.1	BA.2	BA.5	BQ.1.1	XBB.1.5	HK.3.1	BA.2.86	JN.1	epitope group
BD57-1520	BA.1 BTI + BA.5/BF.7	>10,000	>10,000	0.4	2.4	0.2	2.8	2.2	6.2	0.9	6.2	D4
BD57-2225	BA.1 + BA.5/BF.7 (no vaccination)	>10,000	1.6	0.2	0.3	0.4	0.9	0.3	101	0.7	1.0	B

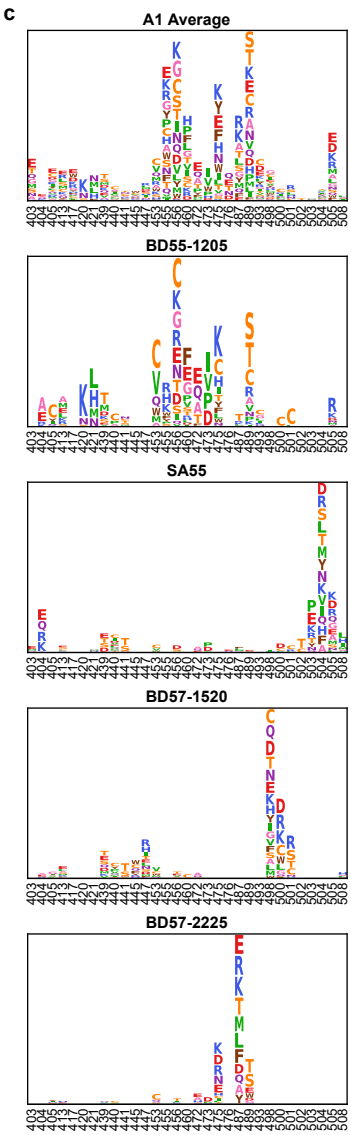

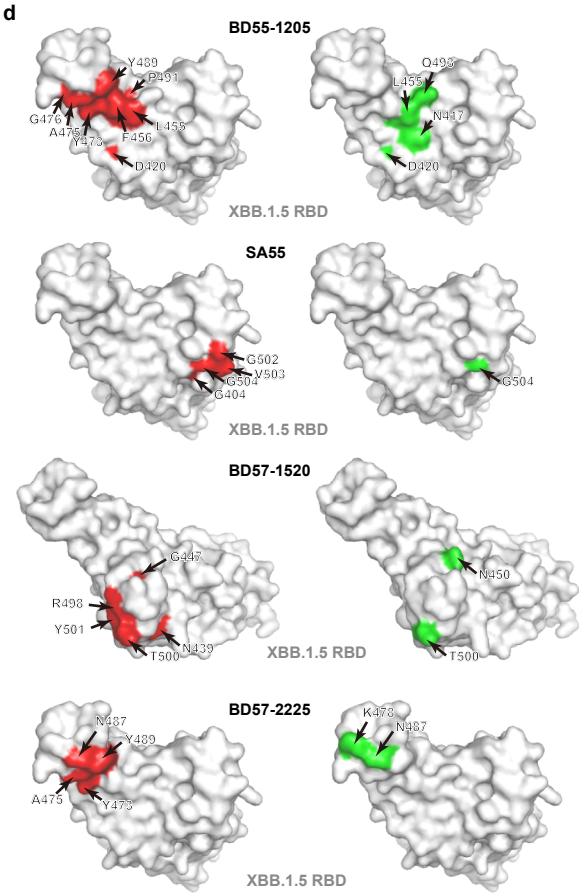

Extended Data Fig. 3 | DMS and rVSV screening indicate the epitopes targeted by bnAbs. a, Schematic for the construction of the SARS-CoV-2 XBB.1.5 Spike-pseudotyped rVSV genome. **b**, Information of the two non-competing NAbs utilized in the rVSV screening assays. **c**, DMS escape profiles (based on BA.5 RBD) of the NAbs involved in the rVSV assays. The average profile of antibodies in epitope group A1 is also shown for comparison with BD55-1205. **d**, Key RBD sites that may be involved in the binding of NAbs (BD55-1205, SA55, BD57-1520 and BD57-2225) as determined by rVSV screening (green) and DMS (red) are marked on the structural model of XBB.1.5 RBD (PDB: 8WRL).

https://doi.org/10.1038/s41564-025-02030-7

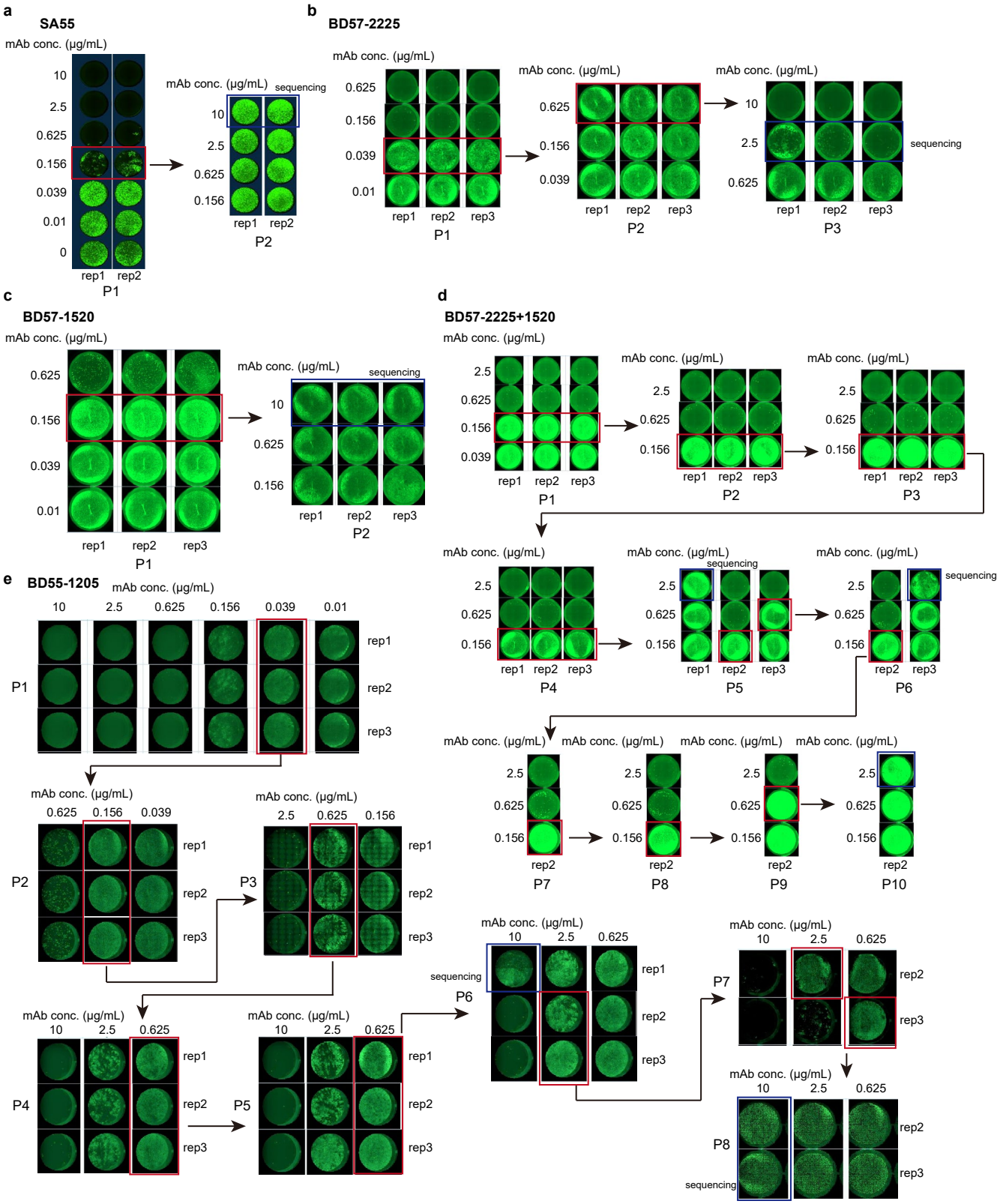

Extended Data Fig. 4 | Raw images of the rVSV escape mutants screening assays. Raw images of the rVSV passages under the pressure of SA55 (**a**), BD57-2225 (**b**), BD57-1520 (**c**), BD57-2225+1520 (**d**), and BD55-1205 (**e**). Red rectangles indicate the well for the next passage, and blue rectangles indicate the well for Sanger sequencing.

https://doi.org/10.1038/s41564-025-02030-7

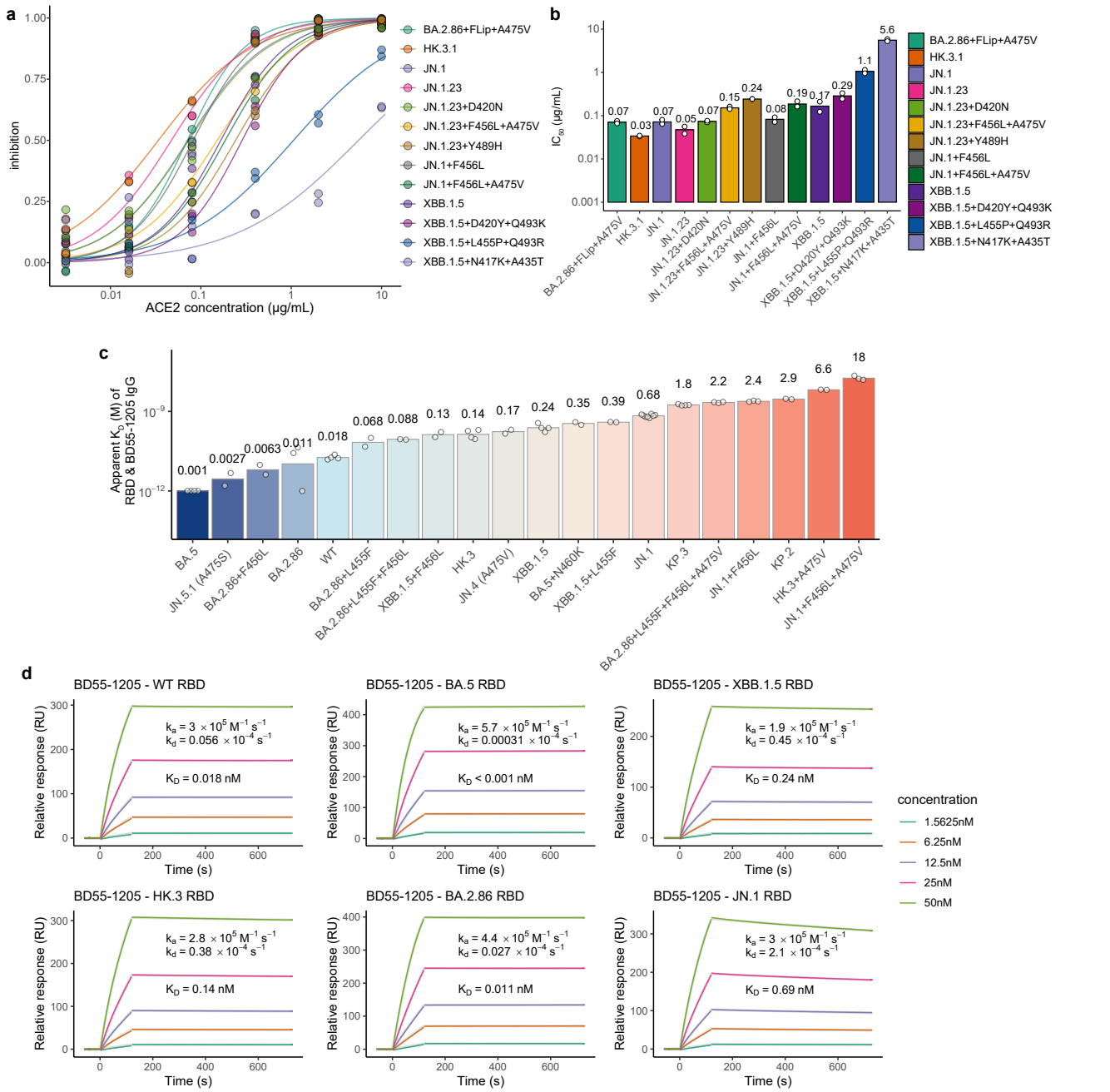

Extended Data Fig. 5 | SARS-CoV-2 variant RBD-binding affinity of BD55-1205 and hACE2. a, Inhibition curves of soluble hACE2 against SARS-CoV-2 Omicron variant pseudoviruses. **b**, IC_{50} of soluble hACE2 against the variants. Geometric mean values are shown and annotated above the bars, and the circles indicate each of two biological replicates. **c**, RBD apparent binding affinity of BD55-1205 IgG to SARS-CoV-2 RBD variants determined by SPR assays. Geometric mean of apparent K_D (nM) is shown and annotated above the bars. Each circle indicates one independent experiment and the number of circles indicate the sample sizes. **d**, SPR sensorgrams of the binding of BD55-1205 to six major SARS-CoV-2 RBD variants. The association and dissociation kinetic coefficients (k_a, k_d), and the apparent dissociation equilibrium constant (K_D) are annotated.

https://doi.org/10.1038/s41564-025-02030-7

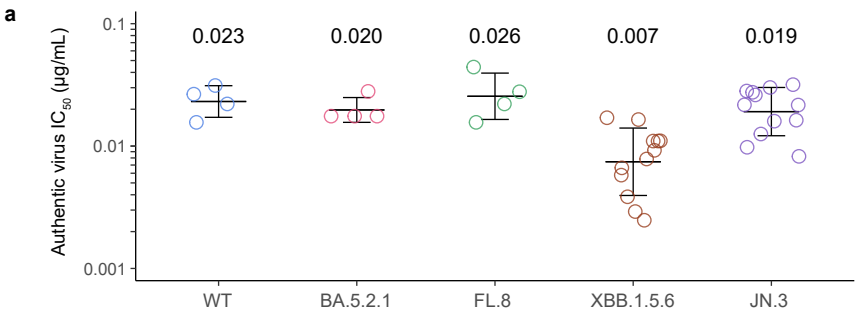

b

Antibody	P1	P2	P3	P4	P5	P6	P7	P8	P9	P10	P11	P12
BD55-1205	4	9	0*	5	0*	3	2.5	12	6	6	6	5

low level CPE

c

		NTD	RBD			S2		
		7	356	360	490	708	1100	1263
		V	K	N	S	S	T	P
Antibody	Passage	G	N	D	Y	F	I	L
BD55-1205	P1	.	.	73.3%	.	.	.	.
	P2	.	.	39.2%	.	.	.	.
	P3	.	42.1%	100.0%	.	.	.	.
	P4	.	.	100.0%	.	.	.	.
	P5	.	.	100.0%	.	.	.	.
	P6	20.2%	.	100.0%	.	.	.	.
	P7	.	.	100.0%	.	.	.	.
	P9	.	.	100.0%	.	48.2%	.	.
	P10	.	.	100.0%	.	.	24.3%	.
	P11	.	.	100.0%	100.0%	.	100.0%	.
	P12	.	.	100.0%	100.0%	.	100.0%	.
	P13	.	.	100.0%	100.0%	.	100.0%	13.5%

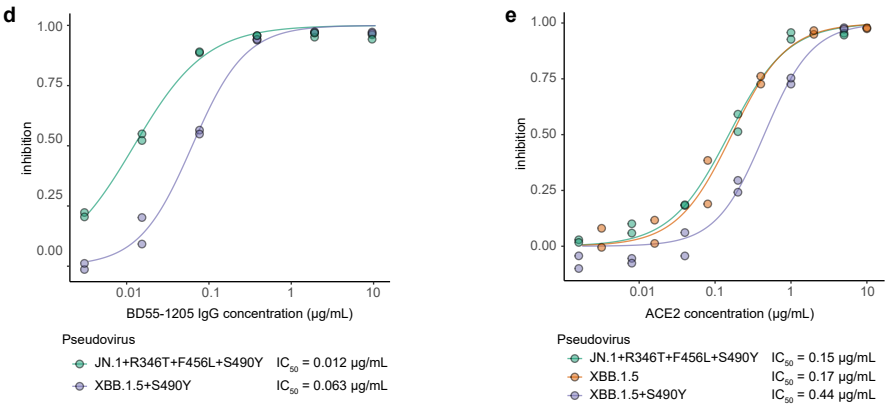

Extended Data Fig. 6 | BD55-1205 inhibits SARS-CoV-2 authentic virus. a, IC50 of BD55-1205 against authentic SARS-CoV-2 isolates WT (n=4), BA.5.2.1 (n=4), FL.8 (n=4), XBB.1.5.6 (n=12), and JN.3 (n=12). Geometric mean IC50 (μg/mL) is labelled above the points and geometric SD is indicated by error bars. Each circle indicates a biological replicate. **b**, Number of wells in the plate that show protection from CPE in each passage in the escape screening assay using XBB.1.5.6 authentic virus. Asterisks indicate low-level/ambiguous CPE observation. **c**, Spike mutations observed in viral S protein resolved using amplicon-based deep sequencing of viral genome at each passage with BD55-1205 selection. **d-e**, Neutralization curves of BD55-1205 (**d**) or soluble hACE2 (**e**) against SARS-CoV-2 Omicron variant pseudoviruses with Spike S490Y mutation. XBB.1.5 inhibition curve is shown here again for comparison. The circles indicate results of two independent replicates.

https://doi.org/10.1038/s41564-025-02030-7

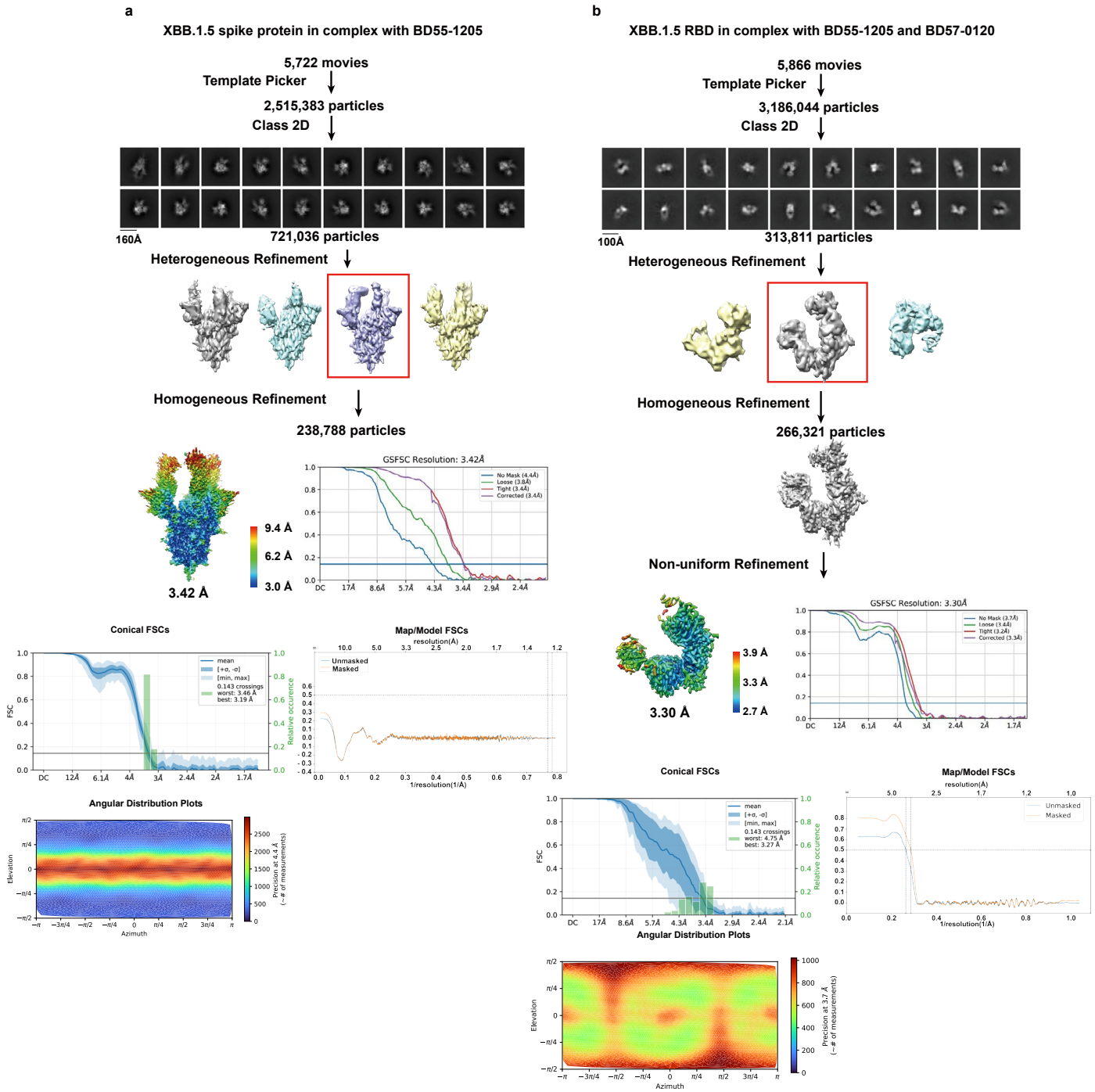

Extended Data Fig. 7 | Workflow for the processing of Cryo-EM data. a, Workflow for the processing of raw Cryo-EM images for XBB.1.5 Spike in complex of BD55-1205. **b**, Workflow for the processing of raw Cryo-EM images for XBB.1.5 RBD in complex of BD55-1205 and BD57-0120.

https://doi.org/10.1038/s41564-025-02030-7

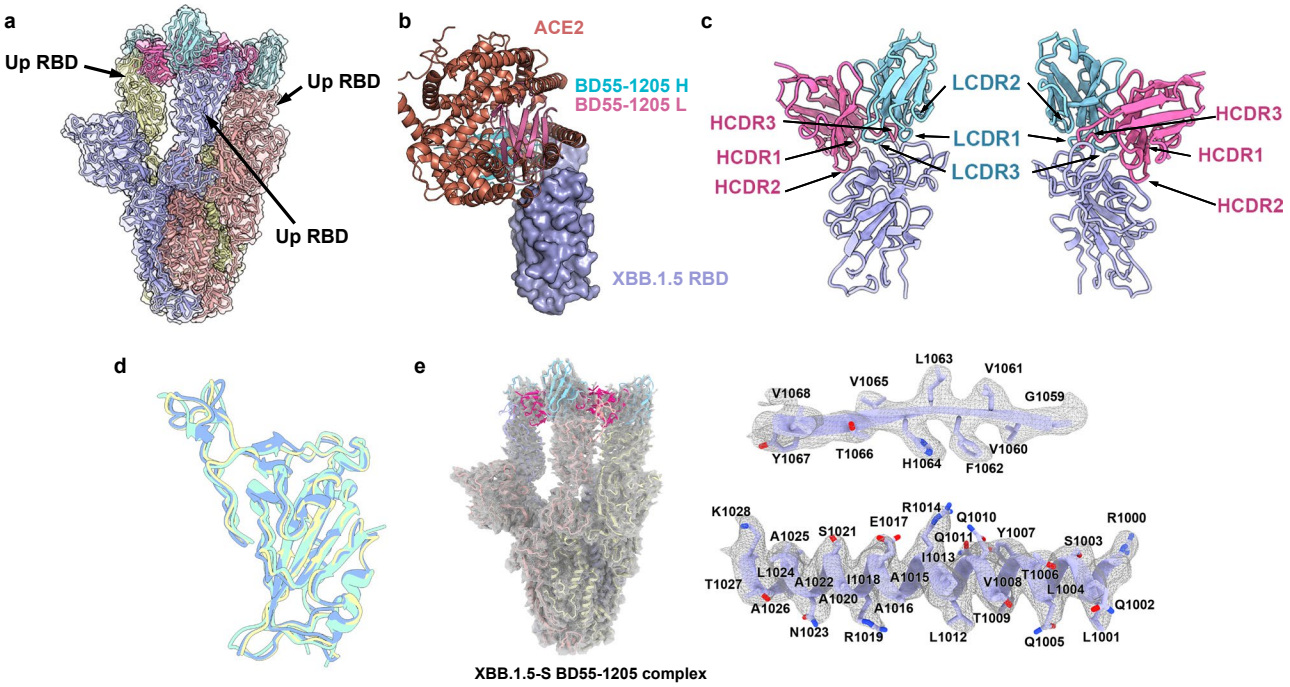

g

	415	416	417	455	456	458	459	460	473	474	475	476	477	487	489	490	491	492	493	501	502	505
WT	T	G	K	L	F	K	S	N	Y	Q	A	G	S	N	Y	F	P	L	Q	N	G	Y
BA.2	T	G	N	L	F	K	S	N	Y	Q	A	G	N	N	Y	F	P	L	R	Y	G	H
BA.5	T	G	N	L	F	K	S	N	Y	Q	A	G	N	N	Y	F	P	L	Q	Y	G	H
BA.2.75	T	G	N	L	F	K	S	K	Y	Q	A	G	N	N	Y	F	P	L	Q	Y	G	H
DV.7.1	T	G	N	F	L	K	S	K	Y	Q	A	G	N	N	Y	F	P	L	Q	Y	G	H
BQ.1.1	T	G	N	L	F	K	S	K	Y	Q	A	G	N	N	Y	F	P	L	Q	Y	G	H
XBB.1.5	T	G	N	L	F	K	S	K	Y	Q	A	G	N	N	Y	S	P	L	Q	Y	G	H
EG.5.1	T	G	N	L	L	K	S	K	Y	Q	A	G	N	N	Y	S	P	L	Q	Y	G	H
FL.1.5.1	T	G	N	L	L	K	S	K	Y	Q	A	G	N	N	Y	S	P	L	Q	Y	G	H
HV.1	T	G	N	L	L	K	S	K	Y	Q	A	G	N	N	Y	S	P	L	Q	Y	G	H
XBB.1.5.70	T	G	N	F	L	K	S	K	Y	Q	A	G	N	N	Y	S	P	L	Q	Y	G	H
HK.3.1	T	G	N	F	L	K	S	K	Y	Q	A	G	N	N	Y	S	P	L	Q	Y	G	H
JF.1	T	G	N	F	L	K	S	K	Y	Q	A	G	N	N	Y	S	P	L	Q	Y	G	H
JD.1.1	T	G	N	F	L	K	S	K	Y	Q	V	G	N	N	Y	S	P	L	Q	Y	G	H
BA.2.86	T	G	N	L	F	K	S	K	Y	Q	A	G	N	N	Y	F	P	L	Q	Y	G	H
JN.1	T	G	N	S	F	K	S	K	Y	Q	A	G	N	N	Y	F	P	L	Q	Y	G	H

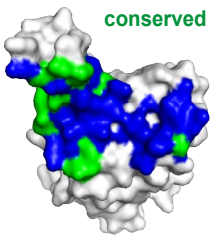

Extended Data Fig. 8 | Structure of BD55-1205 in complex with Spike and RBD. **a**, Structure of BD55-1205 in complex of XBB.1.5 Spike with 3 RBD 'up'. **b**, The epitope targeted by BD55-1205 is highly similar to hACE2 receptor binding sites. **c**, BD55-1205 interacts with XBB.1.5 RBD via heavy chain and light chain CDRs. **d**, Comparison of XBB.1.5 spike protein complex, RBD-BD55-1205-BD57-0120 complex cryo-EM structure, and RBD crystal structure. The RBD from XBB.1.5 spike protein complex (blue, this study), RBD crystal structure (green, PDB 9AU1) were superposed onto RBD double Fab cryo-EM structure (yellow, this study) respectively. The RMSD between RBD crystal structure and double Fab cryo-EM structure is 0.798 Å, and the RMSD between RBD from spike-Fab complex and spike double Fab cryo-EM structure is 0.845 Å. **e**, Cryo-EM density for XBB.1.5 S in complex with BD55-1205 complex and selected β-sheet regions (residues 1059-1067) and α helix (residues 1000-1028). **f**, Overall map of XBB.1.5 RBD in complex with BD55-1205 and BD57-0120 Fab, and representative interaction interfaces are shown. RBD, heavy chain, and light chain are coloured in blue, magenta, and cyan, respectively. **g**, RBD residues in SARS-CoV-2 variants targeted by BD55-1205. Conserved residues are marked in green, and the other residues targeted by BD55-1205 are marked in blue.

https://doi.org/10.1038/s41564-025-02030-7

a

BD55-1205			
Hydrogen bonds			
RBD	H Chain	RBD	L Chain
T415-OG1 ···	S56-OG	R403-NH2 ···	N30-OD1
N417-OD1 ···	Y33-OH	N405-OD1 ···	D93-OD2
D420-OD2 ···	S56-OG	N417-ND2 ···	W94-O
Y421-OH ···	P53-N	Y501-OH ···	N30-O
Y421-OH ···	G54-N	G502-N ···	S28-O
L455-O ···	Y33-OH	H505-ND1 ···	N30-ND2
R457-O ···	P53-O	H505-ND1 ···	G92-O
K458-O ···	P53-O	H505-NE2 ···	N30-ND2
Y473-OH ···	R31-O		
Q474-O ···	R31-NE		
Q474-O ···	R31-NH2		
A475-O ···	N32-OD1		
A475-O ···	N32-ND2		
G476-O ···	T28-OG1	Salt bridges	
N487-OD1 ···	R97-NH1	RBD	L Chain
N487-OD1 ···	R97-NH2	H505-NE2 ···	D93-OD2
N487-ND2 ···	G26-O		
Y489-OH ···	R97-NH2		
Y489-OH ···	E104-OE1		
S490-N ···	R102-NH2		
S490-O ···	R102-NH2		
L492-O ···	R102-NH2		
Q493-OE1 ···	R102-NE		
Q493-OE1 ···	R102-NH1		
Q493-OE1 ···	R102-NH2		

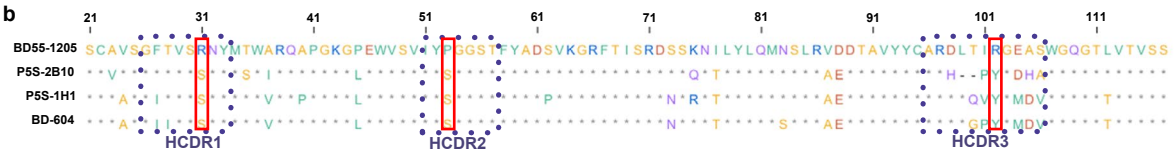

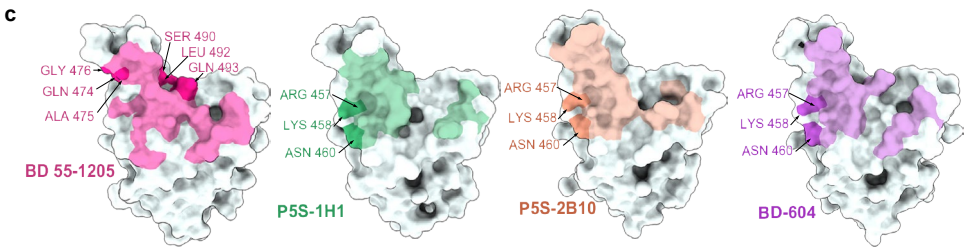

d

Pseudovirus IC_{50} (μg/mL)	BA.5	HK.3.1	JN.1	JN.1 +F456L	JN.1 +F456L +A475V
BD55-1205	0.001	0.006	0.004	0.012	0.021
BD55-1205 (H-R31S)	0.003	0.010	0.007	0.008	0.013
BD55-1205 (H-P53S)	0.003	0.016	0.009	0.008	0.019
BD55-1205 (H-R102Y)	0.002	0.002	0.003	0.009	0.013
BD55-1205-GLHV	0.002	0.005	0.004	0.010	>10

e

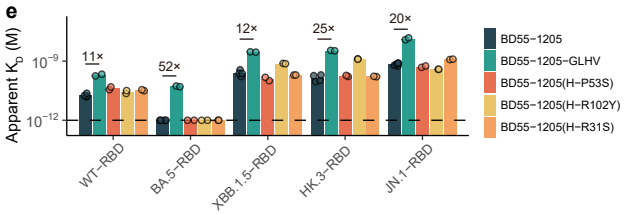

Extended Data Fig. 9 | Comparison of BD55-1205 and Class 1 Nabs. a, A list of all polar interactions between SARS-CoV-2 variant RBD and BD55-1205. Interactions involving RBD backbone atoms are marked in red. **b**, Alignment of the heavy chains of BD55-1205, P5S-2B10, P5S-1H1, and BD-604. Heavy chain CDRs are marked in blue rectangles. Potential key mutations of BD55-1205 are marked in red rectangles. **c**, Footprints of the four antibodies on SARS-CoV-2 RBD. **d**, Neutralization of BD55-1205 with mutations on the heavy chain. **e**, RBD-binding affinity of BD55-1205 with mutations on the heavy chain. Geometric mean values are shown as bars, and each circle indicates one of two independent replicates.

https://doi.org/10.1038/s41564-025-02030-7

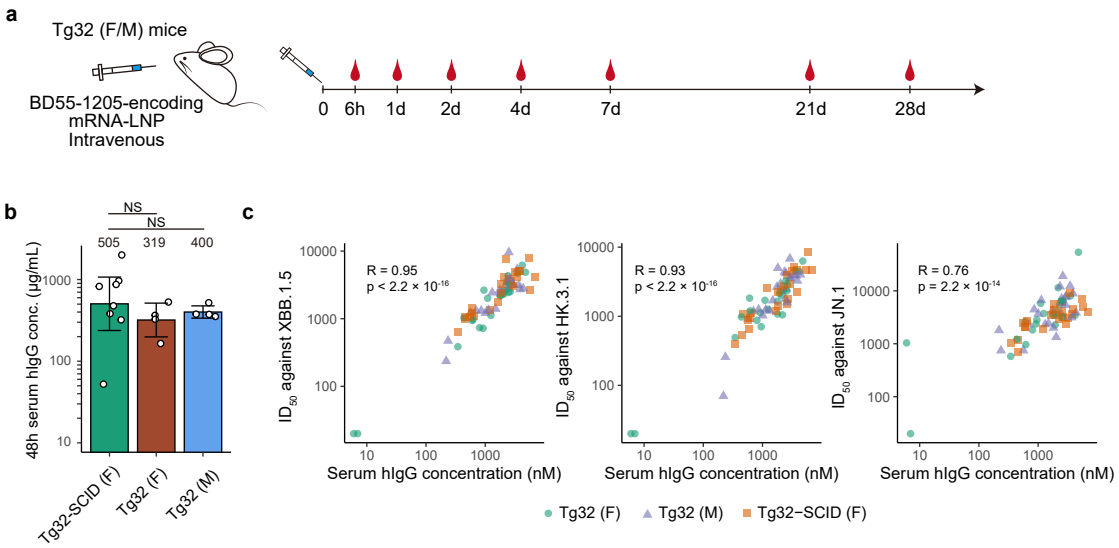

Extended Data Fig. 10 | Immunization of Tg32 mice without SCID. **a**, A schematic of the experimental design for delivery of BD55-1205 in Tg32 mice without SCID. Female (F) or male (M) mice, 4 per group, received 0.5 mg/kg dose by intravenous injection on day 0 and serum was collected at the indicated time points. **b**, Peak serum concentration, occurring at 48 h post LNP administration from the two SCID groups (n=8), and the non-SCID F (n=4) and M (n=4) group. Bar height and number above the bar indicate the geometric mean; error bars indicate 95% confidence intervals; empty symbols indicate individual animals. NS, not significant (two-sided Wilcoxon rank-sum test). **c**, Scatter plots showing the correlation between serum hIgG concentrations and the ID50 against the three variants at indicated timepoints. Pearson correlation coefficients (R) and the corresponding significance p-values are annotated (two-sided t-test).

nature portfolio

Corresponding author(s): Xiangxi Wang, Laura M. Walker, Yunlong Cao

Last updated by author(s): May 6, 2025

Reporting Summary

Nature Portfolio wishes to improve the reproducibility of the work that we publish. This form provides structure for consistency and transparency in reporting. For further information on Nature Portfolio policies, see our Editorial Policies and the Editorial Policy Checklist.

Statistics

For all statistical analyses, confirm that the following items are present in the figure legend, table legend, main text, or Methods section.

n/a	Confirmed	
☐	☒	The exact sample size (*n*) for each experimental group/condition, given as a discrete number and unit of measurement
☐	☒	A statement on whether measurements were taken from distinct samples or whether the same sample was measured repeatedly
☐	☒	The statistical test(s) used AND whether they are one- or two-sided *Only common tests should be described solely by name; describe more complex techniques in the Methods section.*
☒	☐	A description of all covariates tested
☒	☐	A description of any assumptions or corrections, such as tests of normality and adjustment for multiple comparisons
☐	☒	A full description of the statistical parameters including central tendency (e.g. means) or other basic estimates (e.g. regression coefficient) AND variation (e.g. standard deviation) or associated estimates of uncertainty (e.g. confidence intervals)
☐	☒	For null hypothesis testing, the test statistic (e.g. *F*, *t*, *r*) with confidence intervals, effect sizes, degrees of freedom and *P* value noted *Give P values as exact values whenever suitable.*
☒	☐	For Bayesian analysis, information on the choice of priors and Markov chain Monte Carlo settings
☒	☐	For hierarchical and complex designs, identification of the appropriate level for tests and full reporting of outcomes
☒	☐	Estimates of effect sizes (e.g. Cohen's *d*, Pearson's *r*), indicating how they were calculated

Our web collection on statistics for biologists contains articles on many of the points above.

Software and code

Policy information about availability of computer code

Data collection	Pseudovirus neutralization and ELISA data were collected by Multiskan™ FC Microplate Photometer and SpectraMax ABS Microplate Reader (Molecular Devices). Fluorescence data in rVSV-based screening assays were collected by BioTek Cytation 5 Cell Imaging Multimode Reader. SPR data were collected by Biacore 8K Evaluation Software (v4.0.8.20368, Cytiva). Cryo-EM particles data were collected by SerialEM (v4.1).
Data analysis	Data from neutralization assays were analyzed using GraphPad Prism (v8.0 for mice data and v9.0.1 for others). SPR data were analyzed by Biacore 8K Evaluation Software (v4.0.8.20368, Cytiva). Logo plots were generated by Python package logomaker (v0.8). Neutralization and ELISA data are visualized by R package ComplexHeatmap (v2.18.0) and ggplot2 (v3.4.4). Cryo-EM maps and structural models are analyzed and visualized by pymol (v2.6.0a0), Chimera (v1.5), Coot (v0.9.8.91), CryoSPARC (v4.4.1), ResMap (v1.1.4) and Phenix (v1.20.1).

For manuscripts utilizing custom algorithms or software that are central to the research but not yet described in published literature, software must be made available to editors and reviewers. We strongly encourage code deposition in a community repository (e.g. GitHub). See the Nature Portfolio guidelines for submitting code & software for further information.

Data

Policy information about availability of data

All manuscripts must include a data availability statement. This statement should provide the following information, where applicable:

- Accession codes, unique identifiers, or web links for publicly available datasets
- A description of any restrictions on data availability
- For clinical datasets or third party data, please ensure that the statement adheres to our policy

Information of the monoclonal antibodies involved in this study is included in Table S1. Cryo-EM data for structures have been deposited in the Protein Data Bank (PDB) with accession 8XE9 and 8XEA, and in the Electron Microscopy Data Bank (EMDB) with accession EMD-38283 and EMD-38284. Other necessary source data to reproduce the analyses and illustrations have been deposited to Zenedo (10.5281/zenodo.15294998). Additional materials and data are available from the lead corresponding author (Y.C., yunlongcao@pku.edu.cn) upon request and subject to a Material and Data Transfer Agreement. All inquiries will be replied within 7 working days.

Research involving human participants, their data, or biological material

Policy information about studies with human participants or human data. See also policy information about sex, gender (identity/presentation), and sexual orientation and race, ethnicity and racism.

Reporting on sex and gender	This study did not involve human participants.
Reporting on race, ethnicity, or other socially relevant groupings	This study did not involve human participants.
Population characteristics	This study did not involve human participants.
Recruitment	This study did not involve human participants.
Ethics oversight	This study did not involve human participants.

Note that full information on the approval of the study protocol must also be provided in the manuscript.

Field-specific reporting

Please select the one below that is the best fit for your research. If you are not sure, read the appropriate sections before making your selection.

☒ Life sciences ☐ Behavioural & social sciences ☐ Ecological, evolutionary & environmental sciences

For a reference copy of the document with all sections, see nature.com/documents/nr-reporting-summary-flat.pdf

Life sciences study design

All studies must disclose on these points even when the disclosure is negative.

Sample size	The study involves 7,018 SARS-CoV-2 RBD-specific monoclonal antibodies. The sample size is determined by the number of available mAbs in hand and not predetermined. We used four mice in each group of the in vivo study. The number of mice was determined based on experiences from previous studies (https://doi.org:10.1038/s41591-021-01573-6) and sufficient to observe statistical significance. The number is sufficient as validated by the consistency of serum titers within each group.
Data exclusions	668 mAbs were excluded from the study because of insufficient amount of antibody and missing neutralization data against D614G or autologous pseudovirus.
Replication	Experimental assays were performed in at least two independent experiments according to or exceeding standards in the field. Specifically, SPR experiments, live virus neutralization, and rVSV-based screening were conducted in at least two replicates. We used four mice in each group of the in vivo study. Results of all replicates are shown in the figure.
Randomization	Randomization was not required since we were applying a uniform set of measurements across the panel of monoclonal antibodies and plasma. As this is an observational study, randomization is not relevant.
Blinding	Blinding was not required since we were applying a uniform set of measurements across the panel of monoclonal antibodies and plasma, and the experiments were not designed to directly indicate any efficacy. Investigators were not blinded.

Reporting for specific materials, systems and methods

We require information from authors about some types of materials, experimental systems and methods used in many studies. Here, indicate whether each material, system or method listed is relevant to your study. If you are not sure if a list item applies to your research, read the appropriate section before selecting a response.

Materials & experimental systems

n/a	Involved in the study
☐	☒ Antibodies
☐	☒ Eukaryotic cell lines
☒	☐ Palaeontology and archaeology
☐	☒ Animals and other organisms
☒	☐ Clinical data
☒	☐ Dual use research of concern
☒	☐ Plants

Methods

n/a	Involved in the study
☒	☐ ChIP-seq
☒	☐ Flow cytometry
☒	☐ MRI-based neuroimaging

Antibodies

Antibodies used

goat anti-human IgG(H+L)HRP (Bethyl A80-104A)
SARS-CoV-2 nucleocapsid mouse monoclonal antibody (Genscript, A02048)
HRP-coupled anti-mouse IgG secondary antibody (ThermoFisher, 31430)
Custom human antibodies were expressed using Expi293F™ (ThermoFisher, A14527) with codon-optimized cDNA and human IgG1 constant regions in house. The detailed sequences could be found in Supplementary Tables.

Validation

Specificity of custom SARS-CoV-2 RBD-specific mAbs were validated by ELISA and VSV-based pseudotyped virus assays. Details for all SARS-CoV-2 antibodies evaluated in this study is included in Supplementary Table and data from the following published papers:
https://www.nature.com/articles/s41586-023-06753-7
https://www.nature.com/articles/s41586-022-05644-7
https://www.nature.com/articles/s41586-021-04385-3
Commercially available antibodies were validated by the manufacturers as follows:
https://www.fortislife.com/products/secondary-antibodies/goat-anti-human-igg-fc-fragment-antibody/BETHYL-A80-104
https://www.genscript.com/antibody/A02048-SARS_CoV_2_Nucleocapsid_Antibody_4H2_mAb_Mouse.html
https://www.thermofisher.com/antibody/product/Goat-anti-Mouse-IgG-H-L-Secondary-Antibody-Polyclonal/31430

Eukaryotic cell lines

Policy information about cell lines and Sex and Gender in Research

Cell line source(s)

Monoclonal antibody expression: Expi293F™ (ThermoFisher, A14527);
Spike expression for Cryo-EM: FreeStyle™ 293-F (ThermoFisher, R79007);
Pseudutyped virus neutralization assay: Huh-7 (JCRB, 0403) ;
Authentic virus neutralizing assay:Vero(ATCC, CCL-81);
293T(ATCC, CRL-3216);

Authentication

Expi293F™ (ThermoFisher, A14527): https://assets.thermofisher.cn/TFS-Assets/certificate/CM/COA/COA_A14527_3083222_1.pdf;
FreeStyle™ 293-F (ThermoFisher, R79007): https://www.thermofisher.com/order/catalog/product/R79007
Huh-7 (JCRB 0403): https://cellbank.nibiohn.go.jp/~cellbank/en/search_res_det.cgi?ID=385);
Vero(ATCC CCL-81): https://www.atcc.org/products/ccl-81#related-products);
293T(ATCC, CRL-3216): STR profiling (https://www.atcc.org/products/crl-3216)

Mycoplasma contamination

Not tested for mycoplasma contamination;

Commonly misidentified lines
(See ICLAC register)

No commonly misidentified cell lines were used in the study.

Animals and other research organisms

Policy information about studies involving animals; ARRIVE guidelines recommended for reporting animal research, and Sex and Gender in Research

Laboratory animals

Homozygous 'Tg32-SCID' mice (B6.Cg-Fcgrttm1Dcr Prkdcscid Tg(FCGRT)32Dcr/DcrJ cat. no. 018441) and 'Tg32' mice (B6.Cg-Fcgrttm1Dcr Tg(FCGRT)32Dcr/Dry, cat. no. 014565) from Jackson Laboratory were used in this study. The mice are 6-8 weeks old.

Wild animals

No wild animals were used.

Reporting on sex

Only female Tg32-SCID mice are used in the study because the target of this study (delivery of mRNA-LNP and expression of antibodies) should not be significantly affected by sex. Both male and female Tg32 mice are used in the study.

Field-collected samples

No field-collected samples were used.

Ethics oversight	All animal studies were conducted under an Institutional Animal Care and Use Committee (IACUC)- approved protocol (IACUC 23-07-016) in compliance with the Animal Welfare Act, Public Health Service policy, and other applicable state and city public laws and regulations. Animal studies are designed and executed following guidelines from the Guide for the Care and Use of Laboratory Animals 8th Ed.

Note that full information on the approval of the study protocol must also be provided in the manuscript.

Plants

Seed stocks	N/A
Novel plant genotypes	N/A
Authentication	N/A